

IterSIMP- σ : Evaluating LLM-Assisted Spatial Interventions in Stress-Aware Topology Optimization

Shaoliang Yang¹, Jun Wang^{*1}, and Yunsheng Wang¹

¹Department of Mechanical Engineering, Santa Clara University, Santa Clara, CA 95053, USA

Abstract

This paper studies whether multimodal large language models (LLMs) can serve as inspectable spatial proposal modules for stress-aware topology optimization. IterSIMP- σ keeps the SIMP optimizer as a compliance-minimizing finite-element solver and places a deterministic stress pass, gate evaluator, and hybrid LLM/rule interpreter around it. After each solve, density and von Mises stress fields are rendered; the interpreter proposes ranked spatial interventions; and deterministic safeguards accept, reject, or stop each action. The main action is a soft density seed, where selected elements are initialized at elevated density before the next solve but remain free under the optimality-criteria update. We evaluate the loop on a 16-problem 2D controller-policy benchmark, a six-problem exploratory 3D extension, passive-solid and input ablations, stress-threshold sensitivity, and a fixed-volume attribution study comparing LLM proposals with deterministic max-stress hotspot seeding, random stress-region seeding, and rule-based control. The 2D controller-policy benchmark shows a small retained-compliance difference (1.9% lower geometric mean for the soft-seed LLM), but this diagnostic is not statistically significant ($W = 33$, two-sided $p = 0.382$) and is not a fixed-volume feasible-final comparison. In the fixed-volume study, the LLM condition completed 44/48 attempted evaluations; 25/44 completed evaluations produced all-gate-passing retained states. Feasible-final scoring against rule-based control is split 4/4/1, and deterministic exact-hotspot seeding remains competitive. Accepted LLM spatial actions with per-step records have mean normalized seed-to-hotspot distance 0.221. The results support IterSIMP- σ as an inspectable LLM-assisted design-automation framework for spatial interventions, not yet as evidence that LLM visual reasoning improves stress-constrained optimization.

Keywords: Design automation; large language models in design; topology optimization; stress-aware design; SIMP; spatial design intervention

1 Introduction

Topology optimization is a core computational design methodology for distributing material within a prescribed design domain to improve structural performance under volume, manufacturing, and increasingly strength-related requirements [1, 2]. Early homogenization work helped establish material-layout optimization as a structural-design tool [3]. The Solid Isotropic Material with Penalization (SIMP) method remains one of the most widely used density-based formulations because it combines finite-element analysis, penalized stiffness interpolation, filtering, projection, and optimality-criteria updates in a computationally efficient design loop [1, 4–7]. Even in compliance-only settings, the final topology depends strongly on continuation choices such as penalization, filter radius, projection sharpness, move limits, and stopping criteria.

*Corresponding author. E-mail: jwang22@scu.edu

These choices are often treated as numerical details, but in practice they shape the designer’s ability to obtain crisp, feasible, and mechanically interpretable layouts [8].

Stress-aware topology optimization makes the design task more difficult. Element-wise stress constraints are numerous, nonlinear, and sensitive to the stress singularity associated with vanishing material density regions [9, 10]. Classical density-based approaches therefore aggregate local stress measures into a smaller set of constraints, commonly through P -norm or Kreisselmeier–Steinhauser functions [10–12]. More recent augmented-Lagrangian and local-constraint methods reduce reliance on aggregation and have enabled large two- and three-dimensional demonstrations, but local stress control remains computationally demanding and sensitive to modeling choices [13–17]. The design consequence is visible: stress-limited layouts often round re-entrant corners, widen thin members, and redistribute load paths relative to compliance-optimal layouts [18, 19].

This paper approaches that visual and geometric character as a design automation opportunity. A structural designer inspecting a density field and a von Mises stress field can often identify a localized stress concentration, infer whether it arises from a sharp corner, underdimensioned member, or asymmetric load path, and propose a targeted geometric modification. Standard continuation schedules and scalar rule-based controllers do not provide that spatial vocabulary. They can change global parameters, but they cannot directly express interventions such as reinforcing a hotspot, widening a stressed member, or redistributing material between low- and high-stress regions.

Machine-learning methods provide one route to using richer field information in topology optimization. Conditional generators and convolutional networks have been trained to predict final topologies from loads, boundary conditions, intermediate density fields, or initial finite-element fields [20–22]. Other approaches embed learned models inside the optimization loop to accelerate convergence or guide intermediate density trajectories [23–25]. These methods show that field-aware learning can improve design workflows, but they usually require task-specific training data and do not expose a human-readable mechanism for proposing local engineering interventions during a solve. Warm-starting methods similarly demonstrate the practical importance of initial density fields, but typically rely on learned priors or precomputed datasets [26–28].

We study a narrower and more inspectable role for multimodal large language models (LLMs): using visual reasoning as an outer-loop spatial proposal module around an existing SIMP solver. Recent multimodal models can interpret images and diagrams in addition to text [29, 30], and LLM-based agents are increasingly used to coordinate engineering design, structural analysis, and optimization workflows [31–35]. For stress-aware topology optimization, the relevant capability is not open-ended design generation. The relevant capability is bounded spatial reasoning: reading density and stress-field images, identifying a plausible local design weakness, and returning a structured intervention that a deterministic optimizer can accept, reject, or evaluate.

1.1 LLM vision as spatial reasoning for topology optimization

The technical question motivating this work is whether an LLM can (i) localize stress concentrations from a rendered von Mises stress field, (ii) relate those concentrations to the current density topology, (iii) propose geometry modifications with usable spatial coordinates, and (iv) express those modifications in a form that the SIMP optimizer can exploit without surrendering its gradient-based degrees of freedom.

In prior work, we studied an LLM-based adaptive continuation controller for compliance-only SIMP [36], and a natural-language topology-optimization pipeline that can configure, solve, and validate structural problems [37]. The compliance-controller setting used a single density-field image per design step and did not perform stress-localized geometry intervention. Stress-aware spatial control requires a different capability: the controller must read two fields simultaneously,

identify the spatial location of stress violations, and propose geometry changes that are precise enough to resolve local concentrations without disrupting global load paths.

1.2 Contributions

This paper makes the following contributions for design automation and topology optimization:

- (1) **Dual-image LLM interpreter for stress-aware SIMP.** We introduce a stress-aware LLM interpreter that accepts two simultaneous visual inputs per design step: the element density field and the per-element von Mises stress field. The controller can therefore use observed stress concentrations, stress concentration factors, and constraint-violation status when proposing geometry modifications. We add three stress-aware spatial action types: hotspot reinforcement, stressed-member widening, and material redistribution.
- (2) **Controlled soft-seed/passive-solid materialization study.** We compare a seed-biased initialization strategy in which LLM-proposed regions are initialized at elevated density but remain subject to the optimality-criteria update against a passive-solid variant that freezes LLM-placed material. The three-condition ablation (Section 6) makes the central mechanistic tradeoff explicit: soft seeding is less restrictive, while passive-solid materialization is the stronger aggregate performer in the reported retained-compliance data.
- (3) **Fixed-volume attribution study with deterministic and input-ablation baselines.** We define a 16-problem two-dimensional stress-gated controller-policy benchmark plus a fixed-volume attribution study that holds the initial volume fraction constant and compares the LLM policy with deterministic max-stress hotspot seeding, random stress-region seeding, rule-based control, and density-only, stress-only, numeric-only, and global-action-only LLM ablations. This is designed to probe whether any apparent LLM advantage persists after material-budget changes are disabled.
- (4) **Direct localization metrics for spatial actions.** For the fixed-volume attribution study, where per-step traces are available, we measure the distance between accepted spatial seed centers and the true numerical max-stress element, overlap with the top 1%, 5%, and 10% stress regions, and next-step stress changes where the trace supports that coupling. These metrics test whether LLM proposals target stress hotspots rather than treating visual examples as qualitative evidence.
- (5) **Benchmark, reproducibility map, and failure-mode analysis.** We report the original 16-problem two-dimensional controller-policy comparison, a six-problem exploratory three-dimensional extension, and a fixed-volume attribution study with explicit source mapping. The benchmark covers cantilevers, bridges, brackets, portal frames, Michell trusses, asymmetric loads, and torsion-loaded 3D domains. Because the LLM uses deterministic decoding, repeat seeds identify solver and controller traces rather than independent LLM samples. We report descriptive per-problem statistics, feasibility-conditioned endpoints, two-sided Wilcoxon tests, geometric-mean ratios, final gate-pass counts, seed-level variance diagnostics, and a validity check for the 3D bridge result.

1.3 Scope and limitations

The present study uses Gemini 3.1 Flash-Lite Preview as the single LLM at temperature $T = 0$ (deterministic decoding). The corresponding model identifier is `gemini-3.1-flash-lite-preview` [38]. The experiments used the preview endpoint available at execution time, and no served-model revision metadata was retained. The repeat seeds are recorded with each run; in the current implementation, deterministic solver paths begin from a uniform volume-fraction

density, so seed-level variation is limited to paths where the controller or solver state differs across repeats. Archived records support code-level replay of solver and controller state, but not exact replay of the original hosted-model calls. The 3D benchmark provides an exploratory three-seed controller comparison against a rule-based baseline (Section 5.6). This comparison should be interpreted as policy-level evidence rather than an isolated estimate of the seed mechanism: the reported 3D subset does not include a no-seed 3D ablation, fixed-volume attribution studies, or separately calibrated 3D stress thresholds.

The sensitivity of results to the σ_{yield} threshold is characterized across six percentile levels, but repeated runs are reported only at the 50th percentile. The fixed-volume 2D attribution study adds deterministic numerical hotspot seeding, random stress-region seeding, density-only, stress-only, numeric-only, and global-action-only LLM ablations, plus direct hotspot-localization measurements. These runs are the most direct attribution diagnostic because they hold volume fraction fixed and score feasible-retained, feasible-final, and retained-any endpoints separately while reporting execution completeness separately from design feasibility. They are not pooled with the original controller-policy comparison because they use a separately calibrated $\sigma_{\text{yield}} = 163.457$ stress threshold rather than the original $\sigma_{\text{yield}} = 120.3$ threshold; the former was recomputed on fixed-volume attribution reruns under the volume-lock protocol, whereas the latter comes from the original controller-policy trace population. The controller-policy result should therefore be read as a benchmark diagnostic, while the fixed-volume study is the more controlled test of whether LLM spatial proposals outperform deterministic stress-field baselines. The manuscript still does not include a P -norm, K-S, or augmented-Lagrangian stress-constrained solver baseline, fixed-volume 3D reruns, or exact hosted-model replay meta-data.

1.4 Paper organization

Section 2 reviews related work. Section 3 describes the IterSIMP- σ architecture. Section 4 defines the benchmark and protocol. Section 5 reports the main controller-policy results, beginning with the 2D benchmark comparison and followed by the fixed-volume attribution study, sensitivity analysis, convergence behavior, and the 3D benchmark. Section 6 presents the ablation study. Section 7 discusses the operating window and failure modes. Section 8 concludes.

2 Related Work

2.1 Topology optimization under stress constraints

Stress-constrained topology optimization has a long and technically rich history rooted in the observation that compliance-minimizing designs routinely violate local strength criteria. Duysinx and Bendsøe [9] introduced ε -relaxation of local von Mises constraints into the SIMP framework, enabling gradient-based solvers to navigate the singularity problem—the degenerate sub-spaces of the feasible design domain in which globally optimal solutions reside but nonlinear programming algorithms cannot converge. Yang and Chen [11] and Le et al. [10] established the P -norm and Kreisselmeier–Steinhauser (K-S) aggregation approaches, which compress the exponentially large set of local constraints into a single global scalar, making the problem tractable at the cost of conservatism: the aggregation bound is always weaker than the element-wise bound it approximates.

Holmberg et al. [12] addressed the gap between aggregated and local stress control through element clustering, partitioning the domain into groups of stress evaluation points and applying a modified P -norm within each cluster. Bruggi and Duysinx [18] studied the interplay between compliance and stress objectives, showing that minimum-weight designs under stress constraints differ qualitatively from compliance-optimal topologies. Giraldo-Londoño and Paulino [19] unified the treatment of multiple failure criteria (von Mises, Drucker–Prager, Tresca) within a single

topology optimization framework. Applied to the L-bracket and MBB-beam benchmarks—both of which appear in our evaluation—they demonstrated that stress-constrained formulations produce qualitatively different topologies from compliance-only designs, with re-entrant corners replaced by smooth curves. This geometric observation is central to our motivation: the topological difference induced by stress constraints is visually legible, making it a natural target for visual interpretation.

The aggregation-dominated literature was challenged by Senhora et al. [13], who reformulated stress-constrained topology optimization as a mass-minimization problem via the augmented Lagrangian method, preserving the local nature of stress constraints without aggregation. Their approach requires only one adjoint vector regardless of the number of constraints, and produces designs that are consistent under mesh refinement. Xu et al. [39] extended this line to multi-material topology optimization using ordered SIMP interpolation with a stability transformation method to close the gap between the P -norm stress and the exact maximum local stress. Da Silva and Emmendoerfer Jr. [16] recently conducted a systematic comparison of augmented Lagrangian subproblem solvers for stress-constrained topology optimization, confirming the method’s scalability to large 3D problems. A 2024 review [17] surveys the state of the field, noting that local stress control and convergence robustness remain open challenges for density-based methods. Da Silva et al. [14] demonstrated stress-constrained topology optimization at industrial scale with hundreds of millions of local constraints, while Granlund et al. [40] extended stress-constrained formulations to nonproportional loading. Da Silva and Emmendoerfer [41] recently addressed fail-safe stress-constrained design under manufacturing errors. Senhora et al. [15] further advanced the augmented Lagrangian approach to handle continuously varying load directions with local stress constraints.

Beyond density methods, level-set approaches have also been applied to stress-constrained topology optimization. Allaire and Jouve [42] demonstrated minimum-stress design using shape and topological derivatives within a level-set framework. Guo et al. [43] developed a stress-related level-set formulation published in this journal, and Picelli et al. [44] extended the approach to handle P -norm stress aggregation with adaptive constraint scaling. Emmendoerfer and Fancello [45] proposed a reaction–diffusion-based level-set evolution for local stress constraints. Xia et al. [46] addressed stress-based topology optimization using the bi-directional evolutionary structural optimization (BESO) method, demonstrating that discrete design representations avoid the stress singularity problem inherent in intermediate-density formulations. Unlike level-set or BESO formulations, IterSIMP- σ remains density-based: the stress pass is recovered from the penalized SIMP density field and the gate is applied over thresholded solid elements. This makes the stress field operationally useful for gating and visualization, but it is not equivalent to boundary-based stress evaluation.

The present work does not embed stress aggregation in the inner optimizer itself—we retain a post-solve maximum-stress gate over solid elements—but instead uses the LLM to identify and act on stress concentration locations before the optimizer converges, reducing the landscape difficulty that aggregation-based methods face.

2.2 Machine learning and deep learning for topology optimization

The application of neural networks to topology optimization has proceeded along two distinct axes: *data-driven prediction*, which learns a mapping from boundary conditions to optimal topologies using pre-solved training sets, and *optimization acceleration*, which embeds neural networks into the iterative optimization loop itself.

In the prediction line, Yu et al. [20] used conditional generative adversarial networks trained on 100,000 compliance-minimized solutions to predict near-optimal 2D topologies without any solver iterations, demonstrating strong generalization to unseen loads and boundary conditions. Nie et al. [22] introduced TopologyGAN, conditioning the generator not just on boundary conditions but also on the von Mises stress and strain energy density fields from an initial FEA

pass, which is conceptually related to our dual-image approach—though TopologyGAN uses field images as *training input features* rather than as *runtime visual queries* to an agent. Sosnovik and Oseledets [21] trained convolutional encoder-decoder networks to predict final topologies from partially converged intermediate solutions, reducing the number of SIMP iterations required to reach a specified quality level.

In the acceleration line, Deng et al. [23] introduced SOLO, which embeds a deep neural network inside the optimization loop as a dynamically adapting surrogate for the objective function, updating the model only in the region of interest identified by current predictions. Rade et al. [24] developed density sequence (DS) and coupled density–compliance sequence (CDCS) prediction networks that enforce physical consistency by training on intermediate iteration trajectories rather than final solutions only. A 2023 review by Shin et al. [25] provides comprehensive coverage of ML-based topology optimization methods, distinguishing iterative from non-iterative approaches and single-stage from multi-stage architectures.

IterSIMP- σ occupies a distinct position from all of these methods. It does not predict topologies from training data, nor does it substitute a neural surrogate for the FEA computation. Instead, it acts as an *agentic controller* that guides an unmodified SIMP solver through a sequence of geometry modifications—retaining the existing SIMP update structure while adding an outer-loop controller that uses rendered field information.

2.3 Warm-starting and density initialization in topology optimization

The sensitivity of SIMP to density initialization is well established. Uniform initialization ($\rho_e = v_f$) is standard but can trap the solver in suboptimal local minima, particularly under stress constraints where the loss landscape is non-convex and multi-modal.

Data-driven warm-starting has emerged as one strategy to improve initialization quality. Zhang et al. [26] trained a deep generative model on topology optimization solutions and used its predictions as initial density fields, reducing convergence time by 36–58% compared to uniform initialization. Chen et al. [27] proposed conditioning field initialization for neural network-based topology optimization: supplying a strain energy density field computed on the initial domain as an additional input to the density network, improving convergence on problems with complex loading. Kallioras et al. [28] combined SIMP with long short-term memory (LSTM) networks to predict and accelerate the evolution of the density distribution across iterations.

The soft density seed mechanism in IterSIMP- σ differs from these approaches in an important respect: it does not rely on a pre-trained model or a learned prior. Instead, it uses the LLM’s runtime spatial targeting to select seed locations problem-by-problem, warm-starting individual elements at elevated density based on visual identification of stress concentration sites. The mechanism is conceptually closer to *problem-specific initialization guidance* than to data-driven warm-starting, and its contribution is quantified by the three-condition ablation in Section 6.

2.4 LLM agents in engineering design and optimization

Large language models have recently demonstrated broad applicability in engineering design contexts. Makatura et al. [31] conducted a comprehensive survey of LLM-enabled computational design and manufacturing pipelines, showing that general-purpose models (GPT-4) can coordinate existing solvers, algorithms, and visualizers into integrated design workflows without domain-specific fine-tuning. They identified *inverse design* and *topology optimization* as primary candidate domains for LLM augmentation, noting that both require modularisation of hard problems into tractable subproblems—a structure amenable to LLM-guided iteration.

Qin et al. [32] proposed an LLM-based system for shear wall structural design, in which the LLM translates engineer language descriptions into executable optimization code and coordinates a three-level, two-stage topology–pattern–size pipeline. This demonstrates LLM-as-

controller for structural optimization but does not involve visual interpretation of field quantities. For automated structural analysis, recent work [33] used LLMs to parse structural descriptions and generate executable finite-element scripts, with GPT-4o and Gemini Pro as back-end models. In broader optimization contexts, the OR-LLM-Agent framework [34] applied reasoning LLMs to operations research problems through a three-stage pipeline (modelling, code generation, debugging) and showed that structured multi-agent decomposition outperforms single-prompt approaches on complex optimization instances. LLM-driven meta-optimization surveys [35] document the emerging paradigm of LLMs generating, adapting, and evaluating optimization algorithms rather than serving purely as natural-language interfaces.

IterSIMP- σ provides an early controlled evaluation of LLM vision over finite-element density and stress fields as the primary input to a topology-optimization control loop. Our prior work studied an LLM-based adaptive continuation controller for compliance-only SIMP [36], and a natural-language-to-topology pipeline that can autonomously configure, solve, and validate structural problems [37]. The present work builds on that LLM-controlled SIMP direction by introducing dual-image (density and stress) visual reasoning and a soft density seed mechanism for stress-gated spatial intervention. Whereas existing systems use LLMs to generate code, parameterize constraints, or translate natural-language problem descriptions, we use the LLM’s multimodal vision capability to localize stress concentrations in rendered density and stress field images and propose spatially targeted geometry modifications. The empirical evidence distinguishes two effects: the results are consistent with possible benefits from LLM spatial localization on selected cases, while the aggregate soft-seed evidence is mixed and not statistically significant.

3 Method

3.1 System overview

The benchmark IterSIMP- σ loop comprises five modules: SIMP solve, stress pass, evaluator, LLM/rule interpreter, and modifier (Figure 1). A separate Configurator can translate a natural-language problem description into an initial specification in the full workflow, but the quantitative benchmark in Section 4 uses predefined validated problem specifications for repeatability. The Configurator is therefore described for completeness but is not evaluated as a benchmark variable.

Stage 1: One-time configuration. The **Configurator** (LLM-powered, Gemini 3.1 Flash-Lite Preview) translates a natural-language problem description into a validated problem specification $\mathcal{P}^{(0)}$ encoding domain geometry, boundary conditions, volume fraction target, and optional passive or seed regions [37]. This module runs once before the design loop begins and produces the initial input to Stage 2.

Stage 2: Design iteration loop. Five modules execute in sequence at each design step $t = 0, 1, \dots, T_{\max}$:

- (1) **SIMP Solver** (numerical, no LLM). Receives the current specification $\mathcal{P}^{(t)}$ and runs compliance minimization using the SIMP method with an optimality-criteria (OC) update, three-field density filtering, and Heaviside (tanh) projection. The continuation schedule ramps penalization $p : 1 \rightarrow 4.5$, filter sharpness $\beta : 1 \rightarrow 32$, and tightens the minimum filter radius toward $r_{\min} = 1.2$ (Section 3.2). Outputs the converged density field $\boldsymbol{\rho}^{(t)} \in [0, 1]^{n_e}$ and retained compliance $C_{\text{rep}}^{(t)}$.
- (2) **Stress Pass** (numerical, no LLM). Runs a forward FEA pass on the converged stiffness matrix and computes per-element von Mises stress $\boldsymbol{\sigma}^{(t)} \in \mathbb{R}^{n_e}$ (Section 3.3). Both fields

are rendered as 300×300 pixel PNG images $\mathcal{I}^{(t)} = \{\mathcal{I}_\rho^{(t)}, \mathcal{I}_\sigma^{(t)}\}$ for visual input to the Interpreter.

- (3) **Evaluator** (deterministic, no LLM). Applies seven gate checks and four additional diagnostics to the solver output (Section 3.6), producing an evaluation result $\mathcal{E}^{(t)}$ that records which gate checks passed or failed, including the added stress gate $\max_{e:\rho_e > 0.5} \sigma_{\text{vm}}^{(e)} \leq \sigma_{\text{yield}}$. If all seven gate checks pass, the interpreter may stop with the current design as the final output ρ^* .
- (4) **Interpreter** (hybrid LLM/rule module, Gemini 3.1 Flash-Lite Preview, $T=0$). Receives the density image $\mathcal{I}_\rho^{(t)}$, the stress image $\mathcal{I}_\sigma^{(t)}$, the evaluator check results $\mathcal{E}^{(t)}$, the current retained compliance $C_{\text{rep}}^{(t)}$, and the full action history $\{a^{(s)}\}_{s < t}$. It computes deterministic stopping and solver-parameter safeguards, queries the LLM for vision-derived geometry suggestions, and returns a ranked list of candidate actions with structured JSON parameters from the vocabulary in Table 1. Runs at temperature $T=0$ for reproducibility (Section 3.4).
- (5) **Modifier** (deterministic, no LLM). Applies the first valid action proposed by the Interpreter to produce the updated specification $\mathcal{P}^{(t+1)}$, which feeds the next SIMP Solver iteration. Implements three seed kinds: soft (elevated-density warm start, the soft-seed condition), frozen solid (the passive-solid condition), or void lock (Section 3.5).

The implementation terminates when the interpreter stop rule is satisfied, when no admissible new action remains, or when the step budget $T_{\text{max}} = 5$ is exhausted. The deterministic stop rule requires all seven gate checks to pass, a compliance ratio below 1.05, and sufficient load-path efficiency; repeated or blocked actions can also stop a trace when further progress is not expected. The final output is the selected density field ρ^* and its retained compliance C_{rep}^* . In the full workflow, the optional Configurator and the Interpreter invoke an LLM API. In the reported benchmark runs, the initial specifications are predefined and only the Interpreter invokes the LLM API; the SIMP Solver, Evaluator, and Modifier are purely numerical or rule-based. The recorded traces store rendered inputs, parsed LLM action suggestions, applied or rejected actions, and solver/evaluator states, but not complete hosted-model input/output records or provider response identifiers; exact hosted-model replay and independent reconstruction of the original model outputs are therefore not available from the reproducibility materials. The archived records support code-level replay of the controller and solver state, but not exact replay of those hosted-model calls. Algorithm 1 formalizes the iteration.

Algorithm 1 IterSIMP- σ outer design loop

Require: Problem spec $\mathcal{P}^{(0)}$, step budget T_{\max} , yield threshold σ_{yield}

Ensure: Selected density field ρ^* , retained compliance C_{rep}^*

```

1:  $C_{\text{rep}}^* \leftarrow \infty$ ;  $t \leftarrow 0$ 
2: while  $t < T_{\max}$  do
3:    $\rho^{(t)}, C_{\text{rep}}^{(t)} \leftarrow \text{SIMP SOLVE}(\mathcal{P}^{(t)})$   $\triangleright$  SIMP + Heaviside tail (Sec. 3.2)
4:    $\sigma^{(t)} \leftarrow \text{STRESS PASS}(\rho^{(t)}, \mathcal{P}^{(t)})$   $\triangleright$  one forward FEA (Sec. 3.3)
5:    $\mathcal{I}^{(t)} \leftarrow \text{RENDER IMAGES}(\rho^{(t)}, \sigma^{(t)})$   $\triangleright$  300×300 px PNG pair
6:    $\mathcal{E}^{(t)} \leftarrow \text{EVALUATE}(\rho^{(t)}, \sigma^{(t)}, \sigma_{\text{yield}})$   $\triangleright$  seven gate checks plus four diagnostics (Sec. 3.6)
7:   if  $\text{RETAINED ELIGIBLE}(\rho^{(t)}, C_{\text{rep}}^{(t)})$  and  $C_{\text{rep}}^{(t)} < C_{\text{rep}}^*$  then
8:      $C_{\text{rep}}^* \leftarrow C_{\text{rep}}^{(t)}$ ;  $\rho^* \leftarrow \rho^{(t)}$ 
9:   end if
10:   $\mathcal{A}^{(t)}, s^{(t)} \leftarrow \text{INTERPRET}(\mathcal{I}^{(t)}, \mathcal{E}^{(t)}, \{a^{(s)}\}_{s < t})$   $\triangleright$  deterministic safeguards plus dual-image LLM geometry suggestions
11:  if  $s^{(t)} = \text{stop}$  or  $\mathcal{A}^{(t)} = \emptyset$  then
12:    break  $\triangleright$  interpreter stop rule or no admissible new action
13:  end if
14:   $a^{(t)} \leftarrow \text{FIRST ADMISSIBLE}(\mathcal{A}^{(t)})$ 
15:   $\mathcal{P}^{(t+1)} \leftarrow \text{MODIFY}(\mathcal{P}^{(t)}, a^{(t)})$   $\triangleright$  soft-seed injection (Sec. 3.5)
16:   $t \leftarrow t + 1$ 
17: end while
18: return  $\rho^*, C_{\text{rep}}^*$ 

```

RETAINEDELIGIBLE enforces the solver-side finite-positive-compliance and grayness checks used by the retained-best tracker. The seven gate checks are reported separately unless a feasibility-conditioned endpoint is explicitly used.

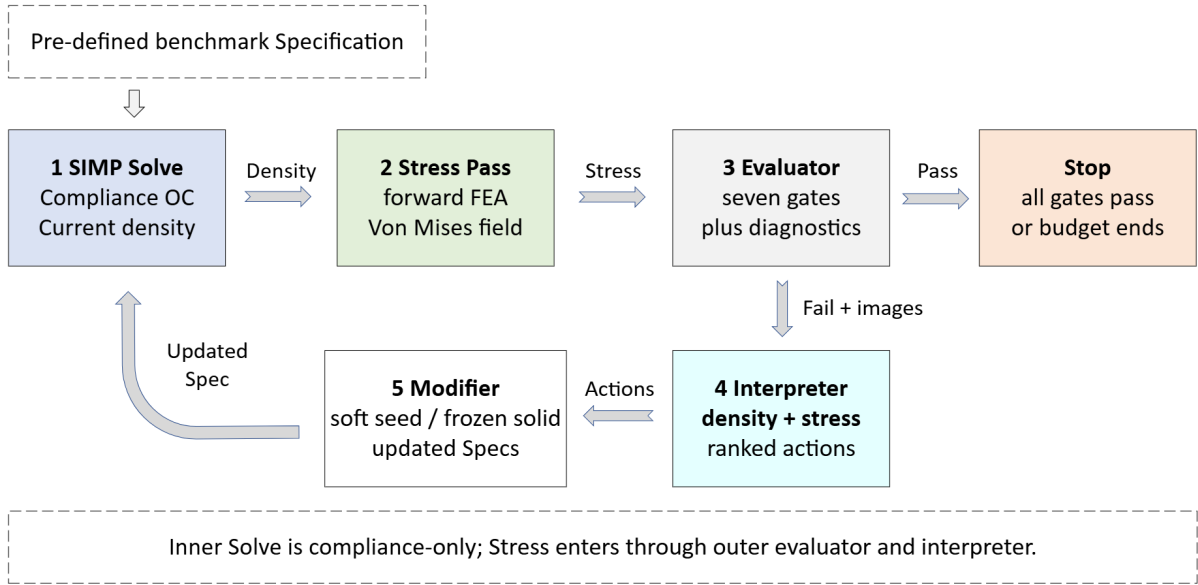


Figure 1: Schematic overview of the benchmark IterSIMP- σ loop. The inner SIMP solve remains a compliance-only OC update. A separate stress pass computes the von Mises field, the evaluator applies seven gate checks plus diagnostics, and the LLM/rule interpreter receives the density and stress images with gate status to propose ranked actions. The modifier applies the first admissible action as a soft seed, frozen solid, or other specification update before returning to the SIMP solve. The loop stops when all seven gates pass, no admissible action remains, or the step budget is exhausted.

3.2 SIMP solver and continuation schedule

The SIMP solver minimizes structural compliance $C = \mathbf{u}^\top \mathbf{K}(\boldsymbol{\rho}) \mathbf{u}$ subject to a volume constraint $V(\boldsymbol{\rho}) \leq v_f V_0$, using the standard optimality-criteria (OC) density update with a three-field (density-filtered density-projected density) formulation [6, 7]. The element stiffness matrix is penalized as $\mathbf{K}_e = \rho_e^p \mathbf{K}_e^0$, with p ramped from 1.0 to 4.5 over the main solve. Heaviside projection with sharpness parameter β is doubled every ten iterations after the penalty ramp, reaching $\beta = 32$ in the main loop and held at $\beta = 32$ throughout the standardized 40-iteration tail-refinement phase common to all conditions. The filter radius r_{\min} is tightened from its initial value toward $r_{\min} = 1.2$ during the late main loop and fixed at that value for the tail. Maximum solver iterations per design step: 120 (2D), 80 (3D).

Seed elements (Section 3.5) receive their initial density assignment immediately before the first OC update of each solver call. This is a seed-biased reinitialization: each solver call starts from the current volume-fraction density except that selected seed elements are initialized at elevated density. The subsequent OC dynamics are unconstrained.

3.3 Stress field computation

After each SIMP solve, one additional forward FEA pass recovers the full displacement field \mathbf{U} under the same stiffness matrix. Strains are evaluated at the element centroid using the \mathbf{B} -matrix of the bilinear quadrilateral (2D, plane-stress) or trilinear hexahedral (3D) element:

$$\boldsymbol{\varepsilon}^{(e)} = \mathbf{B}_e \mathbf{u}_e, \quad (1)$$

where \mathbf{u}_e collects the nodal displacements of element e . The constitutive modulus uses a fixed SIMP penalization exponent $p = 3$ (independent of the solver’s variable penalty schedule) to evaluate stress:

$$E_e = E_{\min} + \rho_e^p (E_0 - E_{\min}), \quad E_{\min} = 10^{-9} E_0, \quad (2)$$

so that void elements contribute negligible stress rather than creating singular stress concentrations. The 2D plane-stress von Mises stress at element centroid is:

$$\sigma_{\text{vm}}^{(e)} = \sqrt{\sigma_{xx}^2 + \sigma_{yy}^2 - \sigma_{xx}\sigma_{yy} + 3\tau_{xy}^2}, \quad (3)$$

with $[\sigma_{xx}, \sigma_{yy}, \tau_{xy}]^\top = E_e \mathbf{D} \boldsymbol{\varepsilon}^{(e)}$ and \mathbf{D} the plane-stress constitutive matrix. For 3D elements we use

$$\sigma_{\text{vm}}^{(e)} = \left\{ \frac{1}{2} [(\sigma_{xx} - \sigma_{yy})^2 + (\sigma_{yy} - \sigma_{zz})^2 + (\sigma_{zz} - \sigma_{xx})^2] + 3(\tau_{xy}^2 + \tau_{yz}^2 + \tau_{zx}^2) \right\}^{1/2}. \quad (4)$$

The stress field is rendered as a blue-to-red (jet) colormap normalized to the maximum $\sigma_{\text{vm}}^{(e)}$ over solid elements ($\rho_e > 0.5$). This matches the renderer used for the reported traces and should be interpreted as a per-panel qualitative stress visualization rather than an absolute cross-panel color scale. All stress-field panels in this paper use this per-panel normalization unless explicitly stated otherwise; color intensity should therefore not be compared quantitatively across different panels. Both the density image and the stress image are saved at 300×300 pixels (padded with white border) for the Interpreter query. The yield threshold σ_{yield} is calibrated from compliance-only reference solves as described in Section 4.

3.4 Dual-image LLM interpreter

At each design step t the Interpreter submits to the LLM (Gemini 3.1 Flash-Lite Preview, `gemini-3.1-flash-lite-preview`, temperature $T = 0$) a structured prompt containing:

- (i) the density field image $\mathcal{I}_\rho^{(t)}$,
- (ii) the von Mises stress field image $\mathcal{I}_\sigma^{(t)}$,
- (iii) a JSON summary of the current evaluation: which gate checks passed or failed, the four recorded diagnostics, the current compliance $C^{(t)}$, retained compliance C_{rep}^* , and whether the maximum-stress gate is satisfied,
- (iv) the action history $\{a^{(s)}\}_{s < t}$ to prevent action repetition.

The prompt instructs the LLM to: (a) identify the primary structural weakness visible in the density image (disconnected members, over-slender sections, asymmetric load paths), (b) locate the highest-stress region in the stress image and estimate its domain coordinates in $[0, L_x] \times [0, L_y]$, and (c) output a ranked list of JSON action candidates with priority, action type, and spatial parameters. The implementation then validates those candidates, keeps LLM-derived geometry actions ahead of duplicate deterministic geometry proposals, and appends deterministic solver-parameter safeguards such as volume-fraction or continuation-schedule changes when required by the evaluator state. The same deterministic rule layer supplies failed-check labels and the conservative stop rule; the LLM is used for spatial interpretation rather than for overriding validity criteria.

Action vocabulary. Table 1 lists the complete action vocabulary. Actions retained from the earlier compliance-only LLM-SIMP controller study [36] operate on global solver parameters; the three stress-aware actions operate on the spatial density field and are the primary mechanism for hotspot targeting.

Table 1: Complete IterSIMP- σ action vocabulary. Actions marked \dagger are introduced in this framework. Priority 1 = highest; the Interpreter proposes a ranked list and the Modifier applies the first valid action.

Action	Type	Effect
Change volume fraction	global	Increase or decrease target volume fraction
Change filter radius	global	Tighten or loosen r_{min}
Change penalization	global	Adjust SIMP penalty exponent p
Insert passive void	spatial	Insert a passive void (locks $\rho_e = \rho_{\text{min}}$)
Insert frozen solid	spatial	Insert a frozen solid ($\rho_e = 1$, ablation only)
Reinforce stress hotspot †	spatial	Place a soft-seed region centered on the peak-stress solid element; in reported 3D traces, circular seed regions are extruded through depth (default $\bar{\rho}_{\text{seed}} = 0.85$; reported LLM traces use 0.85–0.95)
Widen stressed member †	spatial	Add an overlapping chain of soft-seed circles along a stressed member’s centerline (default $\bar{\rho}_{\text{seed}} = 0.80$; reported LLM traces use 0.80–0.90)
Redistribute material †	spatial	Void a low-stress region; simultaneously soft-seed the corresponding high-stress region (default $\bar{\rho}_{\text{seed}} = 0.85$; reported LLM traces use 0.85–0.95)

Stress-gate fallback. When the stress gate check fails ($\max_e \sigma_{\text{vm}}^{(e)} > \sigma_{\text{yield}}$) and no spatial action can plausibly resolve it within the remaining step budget, the Interpreter may propose a volume-fraction increase to reduce global stress levels before resuming spatial corrections. The Modifier can also compound a spatial action with compatible global changes such as volume-fraction or filter-radius adjustments. Consequently, the reported results are controller-policy outcomes rather than isolated tests of a single spatial seed action.

3.5 Soft density seed mechanism

The spatial actions in Table 1 produce circular or rectangular geometry regions in the problem specification \mathcal{P} . Each region carries a *kind* attribute that determines how the SIMP solver treats the enclosed elements. Three kinds are defined:

- (1) **Void** ($\rho_e = \rho_{\min}$, frozen): elements are locked to near-zero density throughout the solve and excluded from the OC update. Used for holes, cutouts, and load-clearance zones.
- (2) **Solid** ($\rho_e = 1$, frozen): elements are locked to full density and excluded from the OC update. Material is forced into the region regardless of sensitivity. Used only in the passive-solid condition to quantify the cost of removing optimizer freedom. These frozen elements are counted in the reported physical volume-fraction check, but they are not redistributed by the OC bisection; passive-solid results therefore change the optimizer’s feasible design space and are treated as an ablation rather than the main soft-seed mechanism.
- (3) **Seed** ($\rho_e \leftarrow \bar{\rho}_{\text{seed}}$, *not frozen — our method*): elements are initialized at elevated density immediately before the first OC update of the next solver call, then participate in the standard OC update identically to all other elements. The seed density is *not* enforced at any subsequent iteration; the optimizer is free to redistribute material away from the seeded region if sensitivity analysis determines it carries insufficient load.

Formally, let $\mathcal{S}^{(t)} \subseteq \{1, \dots, n_e\}$ be the set of seed elements proposed at step t . The modified OC initialization is:

$$\rho_e^{(0)} \leftarrow \begin{cases} \bar{\rho}_{\text{seed}} & e \in \mathcal{S}^{(t)}, \\ v_f & \text{otherwise (uniform re-initialization)}, \end{cases} \quad (5)$$

and for all $k \geq 1$ the standard OC update applies uniformly:

$$\rho_e^{(k+1)} = \min\left(1, \max\left(\rho_{\min}, \rho_e^{(k)} \cdot \left(\frac{-\partial C / \partial \rho_e}{\lambda}\right)^\eta\right)\right), \quad (6)$$

where λ is the Lagrange multiplier for the volume constraint found by bisection, and $\eta = 0.5$ is the OC damping exponent. In implementation, this OC candidate is clipped by the move limit m : $\rho_e^{(k+1)} \in [\rho_e^{(k)} - m, \rho_e^{(k)} + m]$, with $m = 0.05$ in the standardized tail-refinement phase. Crucially, $e \in \mathcal{S}^{(t)}$ receives no special treatment in Equation (6): the seed-biased density assignment evolves freely under sensitivity analysis from iteration $k = 1$ onward.

This differs from the passive-solid ablation, in which seeded elements are excluded from Equation (6) entirely and contribute to the global stiffness at full modulus E_0 regardless of sensitivity. The practical consequence is that a mis-placed solid seed imposes a geometric constraint that the optimizer cannot escape, whereas a soft seed merely biases the initialization: if the sensitivity analysis determines that the seeded region carries insufficient load, material will be redistributed away from it within a few OC iterations.

Figure 2 illustrates the contrast on the cantilever-with-two-voids benchmark. In this case the passive-solid intervention (left, $C = 91.5$) outperforms the soft-seed intervention (right,

$C = 115.2$), even though the latter preserves optimizer freedom. The example therefore illustrates both the mechanical distinction between the two materialization modes and the reason the passive-solid variant must be reported explicitly rather than treated as a secondary implementation detail.

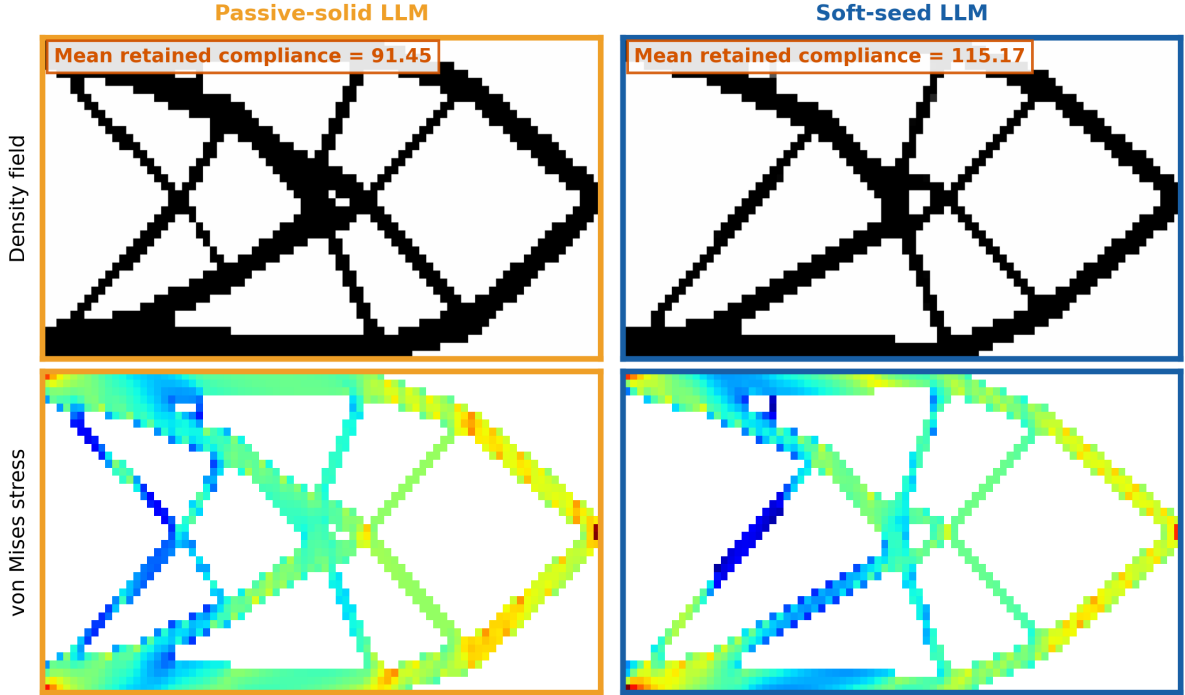


Figure 2: Passive-solid seeding (left) vs. soft density seeding (right) for the cantilever-with-two-voids benchmark. Top row: retained-best density field. Bottom row: von Mises stress field. The passive-solid topology (amber border, $C = 91.5$) has lower compliance than the soft-seed topology (blue border, $C = 115.2$) in the reported experiment. The two panels are seed-42 examples from the same benchmark and compare the retained passive-solid and soft-seed outcomes. They should be read as an illustrative mechanism comparison rather than a controlled same-location intervention, because the realized action sequences differ between the two traces.

Choice of $\bar{\rho}_{seed}$. The seed density must be high enough to bias the initial sensitivity $\partial C / \partial \rho_e$ toward retaining material in the hotspot region (requiring $\bar{\rho}_{seed} > v_f$ for any problem with $v_f < 0.85$), yet not so high as to approach $\rho_e = 1$ and effectively lock the element before the first OC step. We use 0.85 as the default hotspot and redistribution value because it is above every initial benchmark volume fraction while remaining below the frozen-solid limit. The widen-member action uses a slightly lower default seed density ($\bar{\rho}_{seed} = 0.80$) to avoid excessive material commitment along extended flanking regions. In the reported LLM traces, the Interpreter could propose the seed-density parameter; realized values range from 0.80 to 0.95. This parameter variation is part of the reported controller policy, not an isolated fixed-seed-density ablation.

3.6 Stress-gated evaluator

After each solver call the Evaluator applies seven *gate checks* (a failed gate check marks the run as not yet passing and drives the next Interpreter query) and records four *informational diagnostics* (reported but not used for gating). Table 2 lists the gate checks and diagnostics.

The *maximum-stress* gate implements the primary stress constraint:

$$\max_{e: \rho_e > 0.5} \sigma_{vm}^{(e)} \leq \sigma_{yield}. \quad (7)$$

Table 2: Evaluator check suite. Gate checks must all pass for a run to be declared converged. Informational checks are reported but do not gate the loop. Checks marked † are introduced in this framework.

Check	Gate?	Threshold	Definition
Load outside void	Gate	—	No point load inside a passive void region
Connectivity	Gate	≥ 0.99	Fraction of solid elements in largest 8-connected component
Compliance ratio	Gate	≤ 2.0	$C_{\text{final}}/C_{\text{rep}}$
Grayness	Gate	≤ 0.15	$\text{mean}_e \min(\rho_e, 1 - \rho_e)/0.25$
Volume fraction	Gate	$ \Delta v_f \leq 0.05$	Absolute deviation from target v_f
Convergence	Gate	$n_{\text{iter}} \leq 1.5 n_{\text{max}}$	Total solver iterations
Maximum stress †	Gate	$\leq \sigma_{\text{yield}}$	$\max_{e:\rho_e > 0.5} \sigma_{\text{vm}}^{(e)}$
Thin members	Info	—	Fraction of solid boundary elements (erosion proxy)
Checkerboard pattern	Info	—	Fraction of solid elements differing from all 4-neighbours
Load-path efficiency	Info	—	Solid fraction heuristic on direct load path
Stress concentration †	Info	—	$\text{SCF} = \max_e \sigma_{\text{vm}}^{(e)} / \text{mean}_e \sigma_{\text{vm}}^{(e)}$ over solid elements

Only solid elements ($\rho_e > 0.5$) enter this gate, excluding near-void elements where the SIMP-penalized modulus $E_e \approx E_{\text{min}}$ would produce unreliably small stresses. The *stress-concentration factor* (SCF) is reported as an informational diagnostic: a high SCF signals a localized hotspot that the Interpreter should address at the next step, even when the gate passes.

4 Experimental Setup

4.1 Benchmark problems

Table 3 lists all 22 benchmark problems.

4.2 Conditions

The controller-policy diagnostic compares three conditions:

- (1) **Soft-seed LLM (IterSIMP- σ):** LLM interpreter with dual-image input and soft density seeding, starting from predefined benchmark specifications.
- (2) **Rule-based:** identical SIMP solver and tail schedule; no LLM; actions are heuristic scalar adjustments (change volume fraction, change filter radius, change penalization).
- (3) **Passive-solid LLM:** LLM interpreter with dual-image input, but seed regions are frozen as passive solid rather than soft-seeded.

The fixed-volume 2D attribution study adds six further comparisons. These are exact numerical hotspot seeding, random regional seeding, density-only input, stress-only input, numeric-only input, and global LLM action control. The exact-hotspot condition uses the numerical von Mises stress array rather than rendered images to place the same soft-seed intervention around the maximum-stress element. The random condition samples stress-region seed locations with the same spatial-action budget. The input ablations keep the LLM controller but remove parts of the multimodal context or spatial-action freedom. These fixed-volume results are reported separately from the three-condition controller-policy comparison because they address problem-change and localization confounds directly and use a separate 2D stress-threshold calibration.

All conditions use identical SIMP solver settings: maximum 120 solver iterations per design step (capped at 80 for 3D), up to 5 design steps per problem, and a standardized tail-refinement schedule (penalty $p = 4.5$, $r_{\text{min}} = 1.2$, $\text{move} = 0.05$, $\beta = 32$, 40 tail iterations). The volume

Table 3: Benchmark problem suite. All 2D problems use plane-stress elements; 3D problems use trilinear hexahedra. vf = volume fraction. Benchmark label mappings are listed in Appendix A.

ID	Name	Mesh	n_e	vf	Boundary conditions
<i>2D benchmark (16 problems)</i>					
1	Sparse bridge	80×20	1600	0.18	Pin-roller, distributed top load
2	Bridge with circular void	80×20	1600	0.25	Pin-roller, top load, circular void
3	Cantilever with two voids	80×40	3200	0.25	Left fixed, mid-right load, 2 voids
4	Low-volume cantilever	60×30	1800	0.12	Left fixed, mid-right load
5	Asymmetric low-volume cantilever	90×30	2700	0.18	Left fixed, off-axis load
6	Central-void frame	60×60	3600	0.22	Bottom fixed, top-center load, central void
7	L-bracket	40×40	1600	0.30	Top fixed, bottom-right load, upper-right void
8	T-bracket	40×60	2400	0.25	Bottom fixed, right load, left void
9	Simply supported beam	80×20	1600	0.30	Two pin-y supports, mid-top load
10	Portal frame	60×40	2400	0.22	Two corner fixed, distributed top load, central void
11	Asymmetric MBB beam	90×30	2700	0.30	Left pin-x, right bottom pin-y, off-center load
12	Deep beam	60×30	1800	0.35	Pin-roller, distributed top load
13	Michell truss	80×40	3200	0.15	Pin-roller, mid-top point load
14	Basic cantilever	60×30	1800	0.35	Left fixed, mid-right load
15	MBB beam	90×30	2700	0.35	Left pin-x, right bottom pin-y, top-left load
16	Dual-load cantilever	60×30	1800	0.30	Left fixed, two right-edge loads
<i>3D benchmark (6 problems)</i>					
17	3D cantilever	40×20×10	8000	0.25	Left face fixed, mid-right load
18	3D MBB beam	40×14×6	3360	0.18	Left pin-x, right bottom pin-y
19	3D bridge	30×10×6	1800	0.18	Pin-roller, distributed top load
20	3D L-bracket	20×20×5	2000	0.25	Top fixed, bottom-right load, void
21	3D Michell truss	24×12×6	1728	0.12	Pin-roller, mid-top load
22	3D torsion block	20×10×8	1600	0.18	Left fixed, opposing off-axis loads

fraction in Table 3 is the initial benchmark target. Because changing the volume-fraction target is part of the controller action vocabulary, the reported compliance values are outcomes of the corresponding controller policies, not fixed-volume ablations, unless explicitly labeled otherwise. Final volume targets are reported in the 3D table and mapped for all 2D primary traces in Appendix A. Because the benchmark suite is synthetic and author-constructed, it should be read as a controlled stress-gate test bed rather than as a representative sample of all structural design settings.

4.3 Stress threshold calibration

The yield threshold σ_{yield} is calibrated once before the main experiment. Each of the 16 two-dimensional problems is solved in compliance-only mode (no stress constraint, single run), and the peak von Mises stress $\max_e \sigma_{\text{vm}}^{(e)}$ is recorded for each problem. The threshold is then set as a percentile of this distribution: $\sigma_{\text{yield}} = \text{pct}_q(\max_e \sigma_{\text{vm}}^{(e)})$ over the 16 problems. At $q = 50$ (the primary evaluation point) this yields $\sigma_{\text{yield}} = 120.3$ in normalized stress units (consistent with $E_0 = 1$; all quantities are nondimensionalized). This calibration ensures that approximately half the problems fail the stress gate on a compliance-only solve, creating a benchmark where stress-aware intervention has room to contribute without being either trivially satisfied or impossibly tight.

For the 3D benchmark reported here, we retain the same paper-wide threshold $\sigma_{\text{yield}} = 120.3$. This keeps the scalar tables under a single stress gate, but it also means that the 3D results should be interpreted as exploratory controller evidence rather than a separately calibrated stress-active 3D study.

The sensitivity of results to the choice of σ_{yield} is characterized across six percentile levels ($q = 40, 45, 50, 55, 60, 70$) in Section 5.

4.4 Statistical protocol

The primary evaluation is conducted at $\sigma_{\text{yield}} = 120.3$ (50th percentile). Each of the two primary conditions (soft-seed LLM and rule-based) is repeated with three recorded run seeds (42, 123, 7). The current solver initializes most runs from a uniform volume-fraction density; the seeds are retained for run identity and for solver/controller paths that use seeded stochastic state. With deterministic LLM decoding, identical action traces can occur across repeat seeds, so the repeat count should be read as trace-level replication rather than independent LLM sampling. Statistical significance is reported using the two-sided Wilcoxon signed-rank test as the primary inferential check. The corresponding one-sided value in the expected improvement direction is reported only as a directional diagnostic. Problems with coefficient of variation $> 10\%$ are disclosed individually (Section 5.5). Sensitivity to σ_{yield} is characterized across six percentile levels using single runs per condition. Per-problem comparisons are descriptive and are not adjusted for multiple testing.

Retained compliance metric. The scalar result tables report C_{rep} , the compliance value used for comparisons after retaining the best compliance observed across design steps. It is not necessarily the final solver state and, in several 2D cases, it is not a final state satisfying all seven gate checks. We therefore report final gate-pass counts separately from the compliance metric. The final-state compliance is retained separately as C_{final} . When a final logged state satisfies the same finite-positive, grayness, and gate checks as the retained tracker, it is eligible for the reported retained-best value; the 3D bridge rule row below is corrected on that basis. Unless explicitly stated otherwise, scalar tables, classification counts, geometric means, and figure labels use C_{rep} . Standard deviations are descriptive population standard deviations computed over the three repeat-level retained-best compliance values, not inferential uncertainty estimates. A retained candidate must also satisfy the solver-side finite-positive-compliance and grayness eligibility checks used by the retained-best tracker. Because the recorded traces were not generated under a feasibility-conditioned selection rule, C_{rep} is a diagnostic controller-policy metric rather than a feasible-final primary performance metric. The fixed-volume study in Section 5.2 therefore reports feasibility-conditioned retained compliance and feasible-final compliance as primary endpoints. Appendix A maps these reader-facing metrics to the archived summary fields used for reproduction.

5 Results

5.1 2D controller-policy benchmark at $\sigma_{\text{yield}} = 120.3$

In 2D, soft-seed control yields a small non-significant aggregate reduction in retained compliance, with strong problem dependence. Because the comparison is neither fixed-volume nor feasibility-conditioned, this subsection is a controller-policy diagnostic rather than a same-volume performance comparison. Table 4 reports per-problem retained-best compliance (mean \pm population std, $N = 3$ repeats) for all 16 two-dimensional problems at the primary evaluation point $\sigma_{\text{yield}} = 120.3$ (50th percentile), together with the number of repeats whose final evaluator state passes all seven gate checks. These values are controller-policy outcomes; several traces change the final volume-fraction target, as summarized in Appendix A.

Several retained-compliance differences are therefore coupled to large controller-induced volume-fraction changes; Appendix A reports final volume targets, with some cases changing by more than 0.2 absolute volume fraction. This material-budget coupling is why the fixed-volume attribution study is reported separately.

Feasibility-conditioned re-score of existing traces. Table 5 re-scores the same recorded traces under stricter feasibility-conditioned metrics. Runs that never pass all seven gate checks

Table 4: Per-problem retained-best compliance C_{rep} at $\sigma_{\text{yield}} = 120.3$ (calibration percentile $q = 50$), $N = 3$ repeats per condition (seeds 42, 123, 7). Std columns use population standard deviation. Pass columns give the number of repeats whose final state passes all seven gate checks; four additional diagnostics are reported but do not determine validity. Δ : relative retained-compliance difference $= (C_{\text{rule}} - C_{\text{LLM}})/C_{\text{rule}} \times 100\%$.

Problem		LLM mean	pop. std	LLM pass	Rule mean	pop. std	Rule pass	Δ (%)	Guarded class
Asymmetric low-volume cantilever		173.63	11.04	0/3	185.77	0.00	0/3	+6.5	LLM
Sparse bridge		371.89	89.00	0/3	293.40	0.00	0/3	-26.8	Tie
Bridge with circular void		230.87	12.29	0/3	250.82	0.00	0/3	+8.0	LLM
Low-volume cantilever		99.68	4.50	3/3	138.48	0.00	3/3	+28.0	LLM
Basic cantilever		94.76	0.00	3/3	94.76	0.00	3/3	+0.0	Tie
Cantilever with two voids		115.17	1.01	3/3	117.19	0.00	3/3	+1.7	Tie
Deep beam		35.08	0.00	3/3	35.08	0.00	3/3	+0.0	Tie
Dual-load cantilever		288.18	0.74	3/3	291.13	0.00	3/3	+1.0	Tie
Central-void frame		17.61	0.00	3/3	18.26	0.00	3/3	+3.5	LLM
L-bracket		93.92	0.00	3/3	93.99	0.00	3/3	+0.1	Tie
Asymmetric beam	MBB	117.96	5.20	0/3	114.30	0.00	0/3	-3.2	Tie
MBB beam		154.49	0.02	0/3	154.18	0.00	0/3	-0.2	Tie
Michell truss		26.05	3.16	2/3	29.64	0.00	0/3	+12.1	LLM
Portal frame		89.81	10.80	2/3	81.54	0.00	3/3	-10.1	Tie
Simply supported beam		66.26	0.00	3/3	66.26	0.00	3/3	+0.0	Tie
T-bracket		11.88	0.10	3/3	11.95	0.00	3/3	+0.6	Tie

Raw lower means: LLM 9; rule-based 4; equal 3
Guarded class after 3%/std guard: lower LLM 5; lower rule-based 0; ties 11
Geo. mean $C_{\text{LLM}}/C_{\text{rule}} = 0.981$

Retained classes are descriptive; raw means and final gate-pass counts should be interpreted separately. The classes use the practical-tolerance and standard-deviation guard defined in the surrounding text; several mean differences, including three cases with lower rule-based means, are therefore reported as guarded ties. This classification is descriptive and does not override the raw mean differences. Pass counts are not used to assign classes; they separate retained-compliance comparisons from final-state gate-check status. Retained-best states may fail final gate checks, and the controller policies may change the final volume-fraction target.

are marked infeasible and are excluded from the corresponding paired mean rather than contributing a low retained compliance. This re-score checks existing traces; it is not a rerun under a feasibility-conditioned selection rule. It reduces the comparable sample: for C_{feas} , five of the 16 problem pairs are incomplete; for $C_{\text{final,feas}}$, six pairs are incomplete. On the comparable subset, the paired mean counts are lower LLM 7, lower rule 1, equal 3 for feasible retained compliance, and lower LLM 6, lower rule 2, equal 2 for feasible-final compliance.

Statistical test. For the soft-seed LLM condition, a Wilcoxon signed-rank test on the 16 per-problem mean compliance pairs gives $W = 33$, two-sided $p = 0.382$ (one-sided $p = 0.191$). The geometric mean is below one, but this paired test does not provide statistical evidence of a soft-seed advantage.

Guarded descriptive classification. A problem is classified as *lower LLM retained compliance* when the LLM mean compliance is strictly lower than the rule-based mean and the absolute difference $|C_{\text{rule}} - C_{\text{LLM}}|$ exceeds the larger of the two conditions' standard deviations, i.e., $\max(\text{std}_{\text{LLM}}, \text{std}_{\text{rule}})$, and also exceeds a practical 3% compliance tolerance. Problems where the mean difference does not exceed this threshold are classified as ties. Under this criterion, the low-percentage differences for the L-bracket, cantilever with two voids, dual-load cantilever, MBB beam, and T-bracket are treated as practical ties. Three problems have lower rule-based mean compliance (sparse bridge, portal frame, and asymmetric MBB beam), but these are also

Table 5: Existing-trace feasibility-conditioned compliance audit for the 16 two-dimensional primary traces. C_{feas} is the lowest retained compliance among recorded steps passing all seven gate checks. $C_{\text{final,feas}}$ is the final-state compliance when the final state passes all seven gate checks. Entries marked “–” are infeasible under that scoring rule and do not contribute to paired means. The repeats column reports feasible-any/final-feasible counts out of three.

Problem	LLM C_{feas}	LLM $C_{\text{final,feas}}$	LLM reps	Rule C_{feas}	Rule $C_{\text{final,feas}}$	Rule reps
Asymmetric low-volume cantilever	–	–	0/0	–	–	0/0
Sparse bridge	–	–	0/0	–	–	0/0
Bridge with circular void	–	–	0/0	–	–	0/0
Low-volume cantilever	99.68	99.83	3/3	138.48	139.07	3/3
Basic cantilever	94.76	94.76	3/3	94.76	94.76	3/3
Cantilever with two voids	115.17	115.21	3/3	117.19	117.54	3/3
Deep beam	35.08	33.19	3/3	35.08	33.12	3/3
Dual-load cantilever	288.18	288.25	3/3	291.13	291.13	3/3
Central-void frame	17.61	21.93	3/3	18.26	33.44	3/3
L-bracket	93.92	93.92	3/3	93.99	93.99	3/3
Asymmetric MBB beam	–	–	0/0	–	–	0/0
MBB beam	–	–	0/0	–	–	0/0
Michell truss	26.05	26.55	3/2	29.64	–	3/0
Portal frame	89.81	98.54	3/2	81.54	81.54	3/3
Simply supported beam	66.26	66.92	3/3	66.26	66.92	3/3
T-bracket	11.88	15.04	3/3	11.95	16.16	3/3

Retained-any raw lower means: LLM 9; rule-based 4; equal 3.

Feasible-retained paired means, excluding infeasible pairs: LLM lower 7; rule lower 1; equal 3; incomplete 5.

Final-feasible paired means, excluding infeasible pairs: LLM lower 6; rule lower 2; equal 2; incomplete 6.

classified as ties because the differences do not exceed the soft-seed repeat-to-repeat spread.

Figure 3 visualizes all 16 retained-compliance ratios, sorted by effect size, with final gate-pass counts annotated because not all retained-best states are final gate-passing states and some policies change final volume fraction.

Figures 4–6 provide a visual overview of representative seed-42 density fields for all 16 problems. The largest retained-compliance soft-seed differences occur on the low-volume cantilever, Michell truss, bridge with circular void, and asymmetric low-volume cantilever; several difficult geometries are practical ties once a 3% tolerance and seed variability are applied.

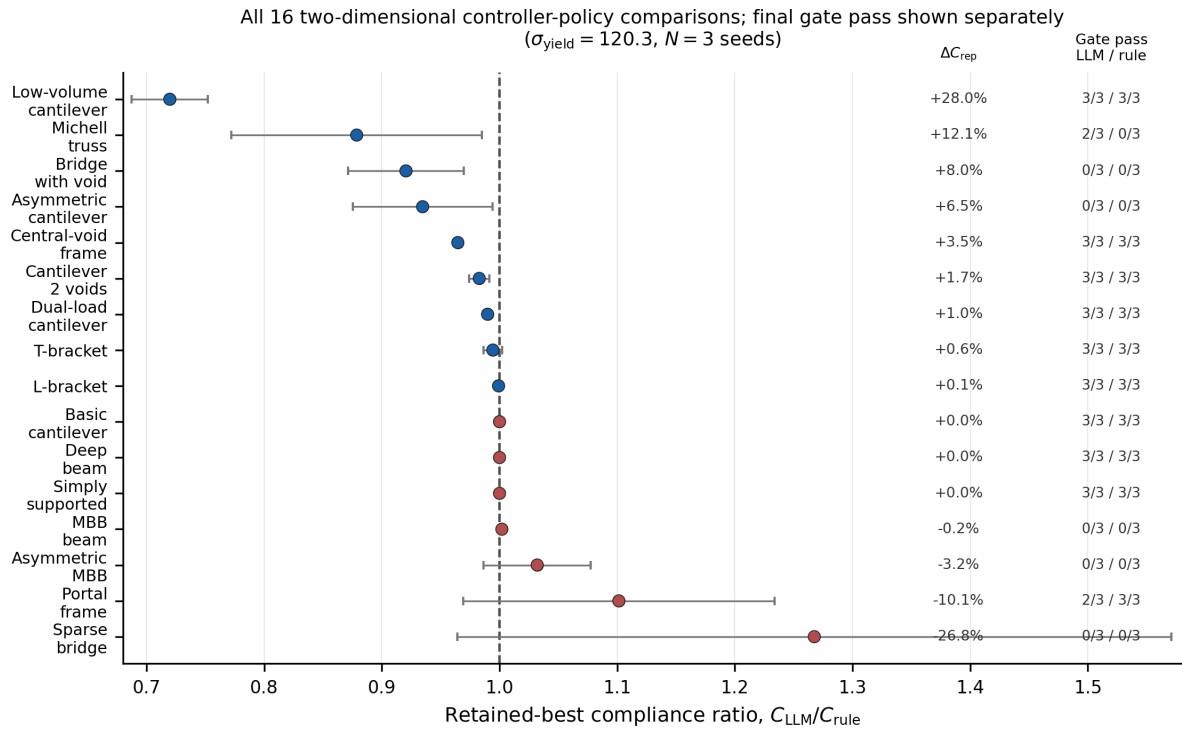


Figure 3: Retained-best compliance ratio for all 16 two-dimensional controller-policy comparisons at $\sigma_{\text{yield}} = 120.3$. Points show $C_{\text{LLM}}/C_{\text{rule}}$ from three-seed mean retained-best compliance; horizontal intervals show the descriptive soft-seed population standard deviation scaled by the rule mean. Values left of one have lower LLM retained compliance, values right of one have lower rule-based retained compliance. Right-side columns report relative retained-compliance difference and final gate-pass counts for LLM/rule repeats.

2D density fields: lower LLM policy retained compliance

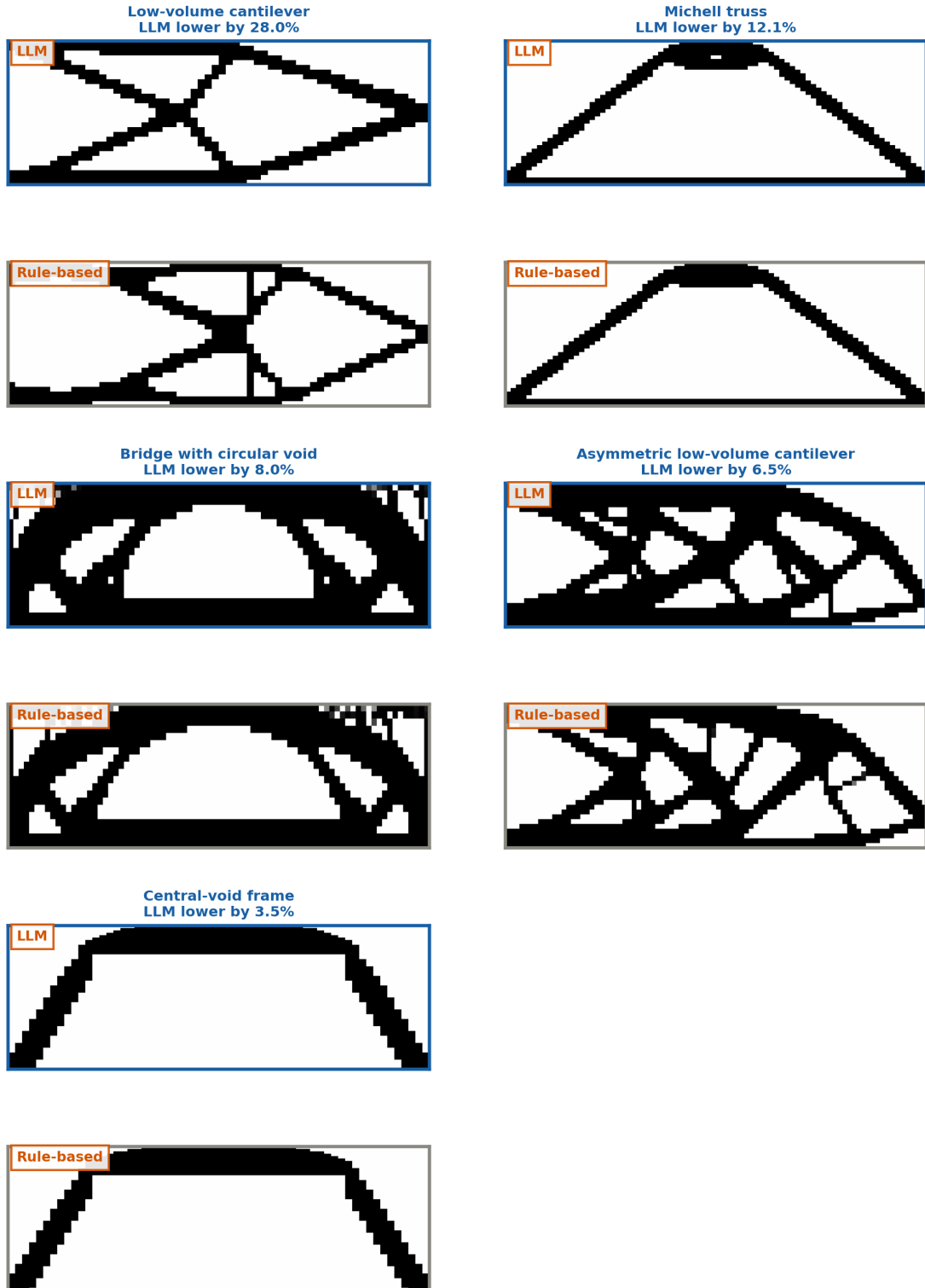


Figure 4: Representative seed-42 density fields for the five two-dimensional benchmark problems classified as lower soft-seed retained compliance after the 3%/std guard ($\sigma_{\text{yield}} = 120.3$). Compliance labels and ordering use three-seed mean retained-best compliance C_{rep} . Each pair shows the LLM topology (blue border, top) and rule-based topology (gray border, bottom). Benchmark label mappings are provided in Appendix A.

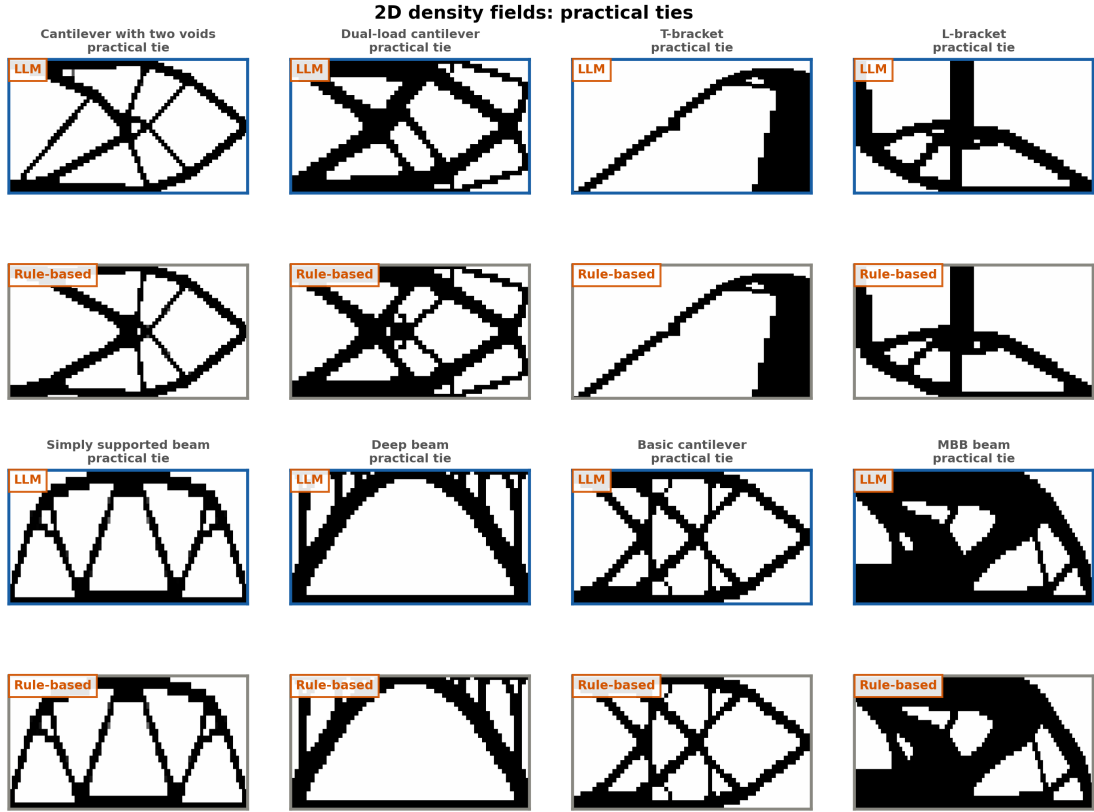


Figure 5: Representative seed-42 density fields for the two-dimensional benchmark cases that are practical ties under the 3% tolerance and seed-variability guard ($\sigma_{\text{yield}} = 120.3$). Compliance labels and ordering use three-seed mean retained-best compliance C_{rep} .

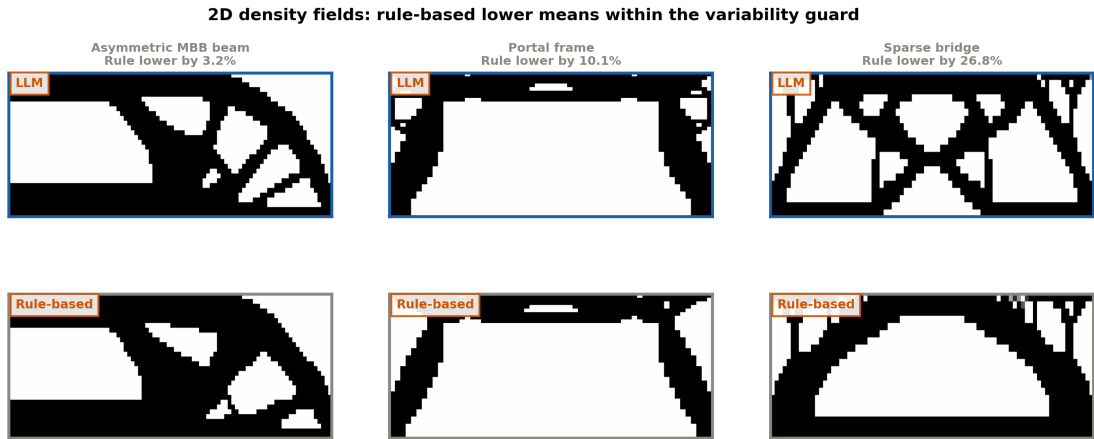


Figure 6: Representative seed-42 density fields for the three cases where the rule-based run has a lower retained compliance mean, but the difference is classified as a guarded tie in Table 4 because it does not exceed the soft-seed variability guard. Compliance labels and ordering use three-seed mean retained-best compliance C_{rep} .

5.2 Fixed-volume hotspot and input-ablation study

The fixed-volume study reruns the 16 two-dimensional problems with the initial volume fraction held fixed throughout the controller loop. It uses a separate 50th-percentile 2D stress calibration, giving $\sigma_{\text{yield}} = 163.457$ for this run. The calibration population is different: the main $\sigma_{\text{yield}} = 120.3$ threshold comes from the historical controller-policy traces whose controllers could change volume fraction, whereas $\sigma_{\text{yield}} = 163.457$ was recomputed for the fixed-volume attribution reruns under the volume-lock protocol. Because this threshold differs from the original controller-policy comparison at $\sigma_{\text{yield}} = 120.3$, these results are not pooled with Table 4. They provide the most direct attribution diagnostic for whether any apparent LLM benefit persists after material-budget changes are disabled.

Tables 6 and 7 score the fixed-volume policies by feasibility-conditioned retained compliance, feasible-final compliance, retained-any compliance, completed-evaluation counts, and trace availability. The fixed-volume study weakens the causal interpretation of the controller-policy retained-compliance difference. The LLM condition completed 44 of 48 attempted problem/repeat slots. Four attempted evaluations did not yield completed designs because execution ended before evaluation; these are reported separately from completed but infeasible designs. The exact-hotspot condition completed 47 of 48 attempted slots, and the rule, random, and input-ablation controls completed all 48. Feasibility is therefore interpreted among completed evaluations, while missing executions are reported separately rather than treated as structural infeasibility. Among completed evaluations, 25 of 44 soft-seed LLM records and 27 of 48 rule-based records produce an all-gate-passing retained state. Seven of the sixteen LLM/rule problem pairs are incomplete for feasibility-conditioned pairwise comparisons. Across the nine complete LLM/rule paired problems, the LLM has lower mean C_{feas} in 5 cases, rule-based control is lower in 0, and 4 are equal within table precision. Feasible-final scoring is split: lower LLM 4, lower rule 4, equal 1. The corresponding geometric-mean ratios versus rule-based control are 0.995 for feasible-retained compliance, 1.002 for feasible-final compliance, and 0.958 for retained-any compliance. Thus the fixed-volume study controls the material-budget degree of freedom but does not show a clear feasible-final LLM performance advantage.

Table 6: Fixed-volume 2D experiment scored by feasibility-conditioned retained compliance. Entries are means over feasible retained repeats. Parentheses report feasible/completed/attempted repeats, so attempted slots that ended before evaluation are separated from completed but infeasible designs. The final column reports the maximum absolute mean final-volume drift from the initial target across the displayed conditions.

Problem	Soft-seed LLM	Exact hotspot	Rule-based controller	Random stress region	Max $ \Delta v_f $
Asymmetric low-volume cantilever	– (0/3/3)	– (0/3/3)	– (0/3/3)	– (0/3/3)	0.000
Sparse bridge	– (0/3/3)	– (0/3/3)	– (0/3/3)	– (0/3/3)	0.000
Bridge with circular void	– (0/3/3)	– (0/3/3)	– (0/3/3)	– (0/3/3)	0.000
Low-volume cantilever	– (0/3/3)	– (0/3/3)	– (0/3/3)	– (0/3/3)	0.000
Basic cantilever	94.75 (3/3/3)	93.87 (3/3/3)	94.75 (3/3/3)	94.75 (3/3/3)	0.000
Cantilever with two voids	134.64 (3/3/3)	135.01 (3/3/3)	135.94 (3/3/3)	135.01 (3/3/3)	0.000
Deep beam	34.17 (3/3/3)	35.08 (3/3/3)	35.08 (3/3/3)	35.05 (3/3/3)	0.000
Dual-load cantilever	– (0/1/3)	– (0/3/3)	– (0/3/3)	– (0/3/3)	0.000
Central-void frame	18.19 (3/3/3)	18.20 (3/3/3)	18.20 (3/3/3)	18.20 (3/3/3)	0.000
L-bracket	93.75 (3/3/3)	93.75 (3/3/3)	93.75 (3/3/3)	93.75 (3/3/3)	0.000
Asymmetric MBB	– (0/3/3)	– (0/3/3)	– (0/3/3)	– (0/3/3)	0.000
MBB beam	– (0/3/3)	– (0/3/3)	– (0/3/3)	– (0/3/3)	0.000
Michell truss	37.96 (3/3/3)	38.38 (2/2/3)	38.38 (3/3/3)	37.57 (3/3/3)	0.000
Portal frame	98.57 (3/3/3)	98.57 (3/3/3)	98.57 (3/3/3)	98.57 (3/3/3)	0.000
Simply supported	66.26 (3/3/3)	66.26 (3/3/3)	66.26 (3/3/3)	66.26 (3/3/3)	0.000
T-bracket	11.96 (1/1/3)	11.96 (3/3/3)	11.97 (3/3/3)	11.97 (3/3/3)	0.000

Table 7: Fixed-volume 2D ablation summary. Completion reports completed evaluations out of attempted condition/problem/repeat slots. Feasibility counts are feasible/completed evaluations, not feasible/all-attempted slots; missing executions are reported separately. Ratios are geometric means versus fixed-volume rule-based control over complete problem pairs. Trace/action counts used for localization diagnostics are reported in Appendix A.

Condition	Completed	Feas. retained	Feas. final	Missing exec.	$C_{feas}/rule$	$C_{final,feas}/rule$	$C_{any}/rule$	Paired problems
Soft-seed LLM	44/48	25/44	25/44	4	0.995	1.002	0.958	9/16
Exact hotspot	47/48	26/47	26/47	1	0.998	1.000	1.000	9/16
Rule-based controller	48/48	27/48	27/48	0	1.000	1.000	1.000	9/16
Random stress region	48/48	27/48	27/48	0	0.997	1.000	0.967	9/16
Density-only LLM	48/48	27/48	27/48	0	0.998	1.001	0.787	9/16
Stress-only LLM	48/48	27/48	27/48	0	0.996	0.997	0.798	9/16
Numeric-only LLM	48/48	27/48	27/48	0	0.994	0.995	0.828	9/16
Global-only LLM	48/48	27/48	27/48	0	1.000	1.000	1.000	9/16

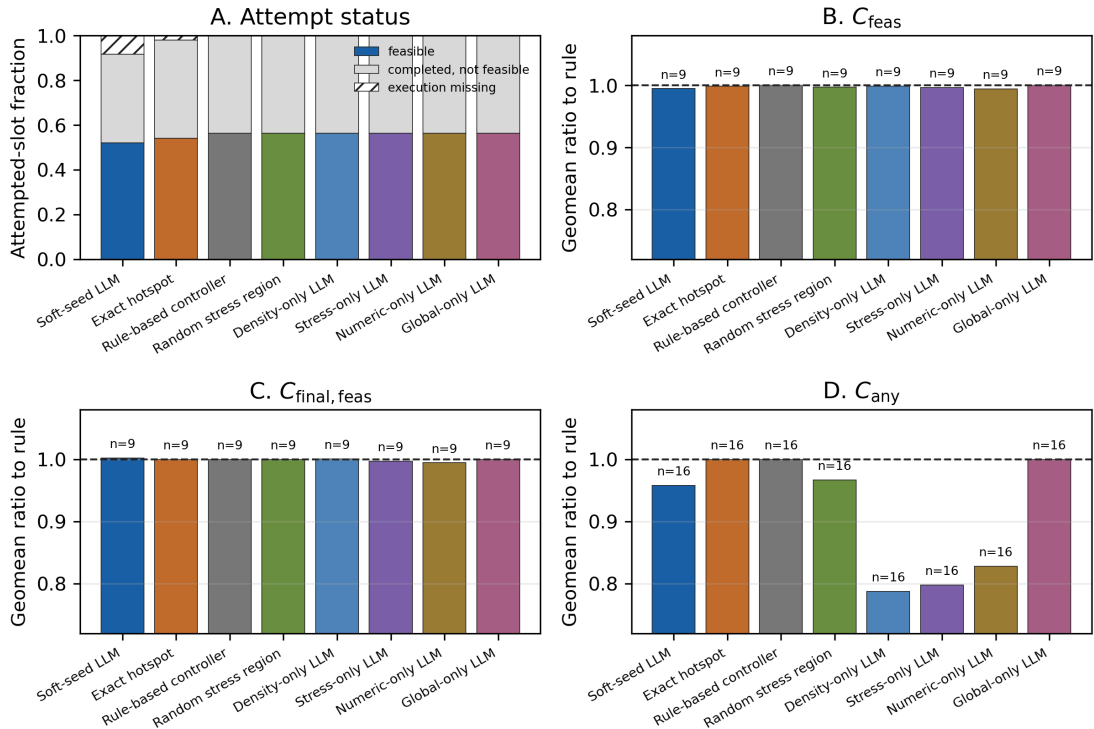


Figure 7: Fixed-volume 2D primary endpoints. Panel A decomposes attempted condition/problem/repeat slots into feasible retained designs, completed but non-feasible evaluations, and missing executions. Panels B–D report geometric-mean ratios to fixed-volume rule-based control for feasibility-conditioned retained compliance, feasible-final compliance, and retained-any compliance, respectively; n gives the number of complete problem pairs used for each geometric mean. Values below one have lower compliance than rule-based control.

The deterministic max-stress hotspot baseline is competitive with the LLM policy under the feasible-primary endpoints. Against exact hotspot seeding, the LLM has lower feasible-retained compliance in 5 of 9 complete paired problems, exact hotspot is lower in 1, and 3 are equal. Under feasible-final scoring, exact hotspot is lower in 5 of the 9 complete paired problems, while the LLM is lower in 4. This comparison addresses the central attribution question: the present data do not show that a vision LLM locates stress interventions better than a simple algorithm using the numerical stress field.

Direct localization metrics lead to the same conclusion, with an important trace-coverage limitation. The recovered seed-7 scalar summary contributes to the completed-evaluation counts above, but its per-step traces were not available for localization/action diagnostics; the LLM localization analysis therefore covers 28 completed evaluations with per-step records. Over 76

accepted LLM spatial actions in those traces, the mean normalized distance between the LLM seed center and the true maximum-stress element is 0.221 domain diagonals. Mean overlap of the seed region with the top 1%, 5%, and 10% stress regions is 0.041, 0.118, and 0.196, respectively. These values show that some LLM proposals intersect high-stress regions, but the localization is not precise enough to establish reliable hotspot targeting. The density-only, stress-only, numeric-only, and global-action-only ablations further show that retained-any compliance can improve without producing a comparable feasible-final advantage. The fixed-volume study therefore improves attribution clarity while weakening any claim that LLM visual reasoning is the causal source of the observed controller-policy differences.

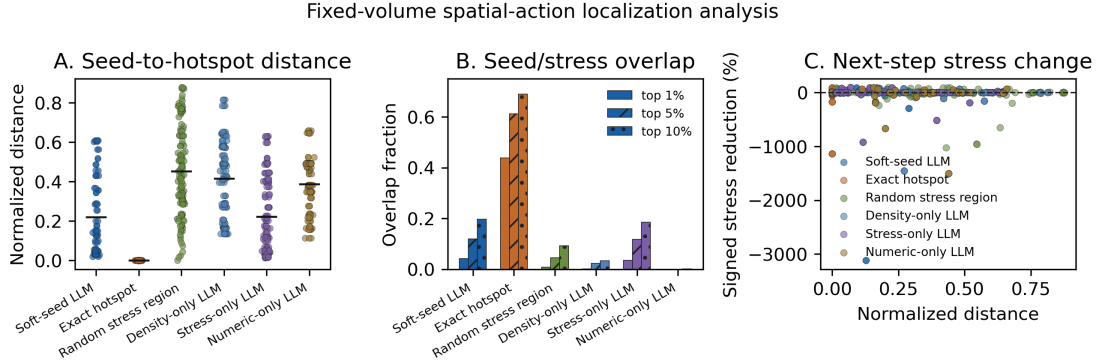


Figure 8: Spatial-action localization analysis across fixed-volume policies. Panel A shows per-action normalized seed-to-hotspot distances with mean bars. Panel B reports seed overlap with the top 1%, 5%, and 10% von Mises stress regions. Panel C couples the accepted spatial action to signed next-step stress reduction, $100(\sigma_{\text{current}} - \sigma_{\text{next}})/\sigma_{\text{current}}$; positive values indicate stress reduction and negative values indicate stress increase. Exact hotspot seeding is the zero-distance reference. The figure uses only completed evaluations with available per-step traces.

5.3 Sensitivity to σ_{yield}

The primary evaluation above is conducted at a single calibration point. Figure 9 and Table 8 report the stress-gate pass count across six calibration levels. These single-seed sweeps are used as calibration evidence only: the deterministic calibration study uses the rule-based interpreter path, so it coincides with the matched rule study. The gate-pass count is 10/16 for both studies from calibration percentile $q = 40$ through $q = 55$, rises to 12/16 at $q = 60$, and reaches 14/16 at $q = 70$ as the stress gate becomes loose.

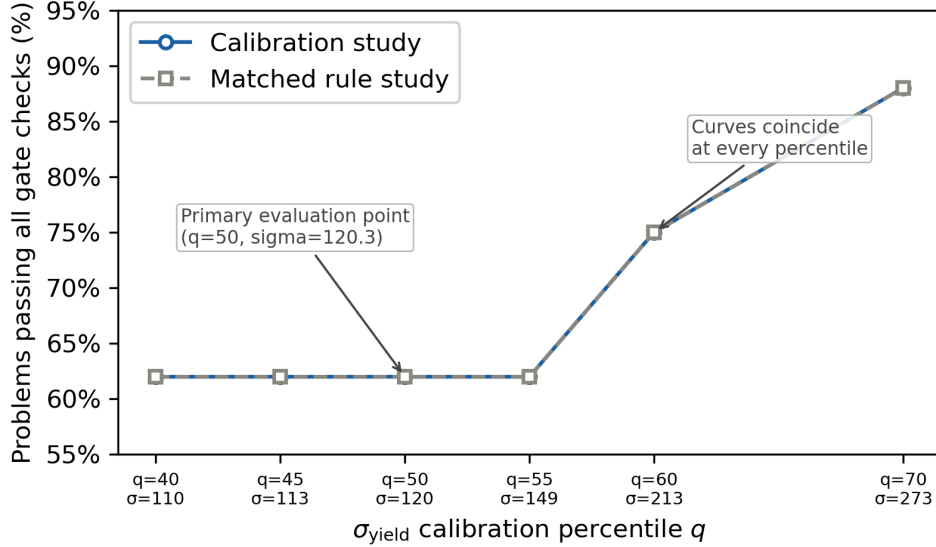
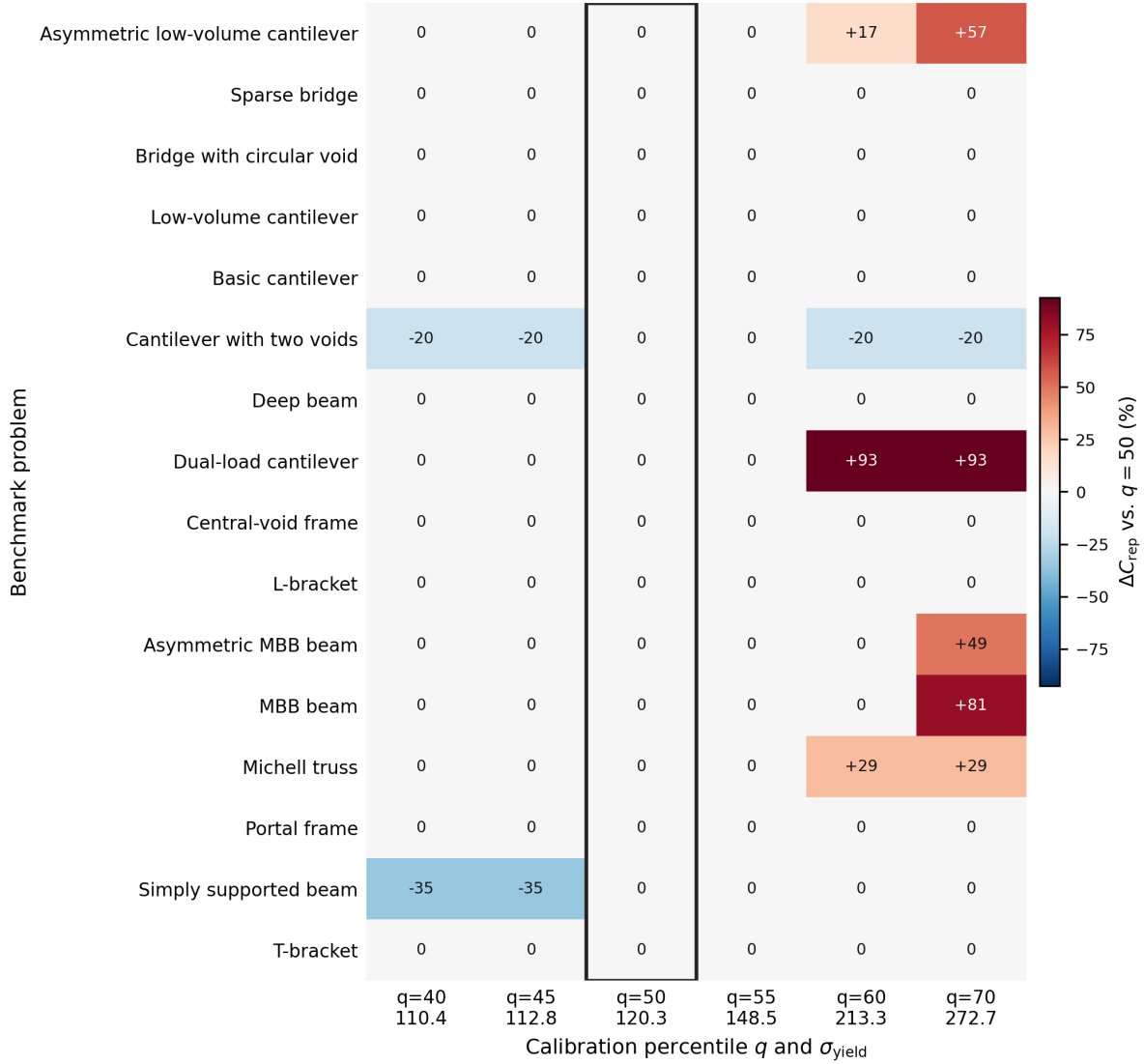


Figure 9: Stress-satisfaction rate vs. σ_{yield} calibration percentile. The deterministic calibration study uses the rule-based interpreter path and therefore coincides with the matched rule study. This figure is calibration evidence, not controller-comparison evidence.

Table 8: Sensitivity of stress-satisfaction rate to σ_{yield} . % fail at initial solve: fraction failing the stress gate on the compliance-only solve. “Gate pass” means all seven evaluator gate checks pass; four diagnostics are recorded but do not gate validity. Single run per condition per calibration level; $N = 3$ repeated runs are reported only at $q = 50$ (primary). Boldface marks the primary evaluation point.

q	σ_{yield}	% fail initially	Calibration study	Matched rule study	Outcome
40	110.4	56%	10/16 (62.5%)	10/16 (62.5%)	Same
45	112.8	56%	10/16 (62.5%)	10/16 (62.5%)	Same
50	120.3	50%	10/16 (62.5%)	10/16 (62.5%)	Same
55	148.5	44%	10/16 (62.5%)	10/16 (62.5%)	Same
60	213.3	38%	12/16 (75%)	12/16 (75%)	Same
70	272.7	31%	14/16 (87.5%)	14/16 (87.5%)	Same

Figure 10 disaggregates the calibration sensitivity analysis to show how each problem’s retained compliance changes relative to the primary $q = 50$ calibration level. Because the sweep is not an LLM-controller run, it should be read as a map of stress-threshold sensitivity rather than evidence for controller benefit.



Calibration study and matched rule study coincide; values are row-wise changes from the primary $q=50$ setting.

Figure 10: Per-problem retained-compliance sensitivity to the σ_{yield} calibration level. Cell values show the percentage change in retained-best compliance C_{rep} relative to the primary $q = 50$ value for the same problem; negative values indicate lower retained compliance than at $q = 50$. The calibration study uses the rule-based interpreter path, so this is calibration evidence rather than an LLM-vs-rule comparison. Problems are sorted by their primary-evaluation ordering, and the boxed column marks $q = 50$, $\sigma_{\text{yield}} = 120.3$.

5.4 Convergence analysis

Figure 11 shows step-by-step compliance for four representative seed-42 traces.

Raw per-step final compliance (faint) and retained running minimum at $\sigma_{\text{yield}} = 120.3$ (seed 42; log scale)

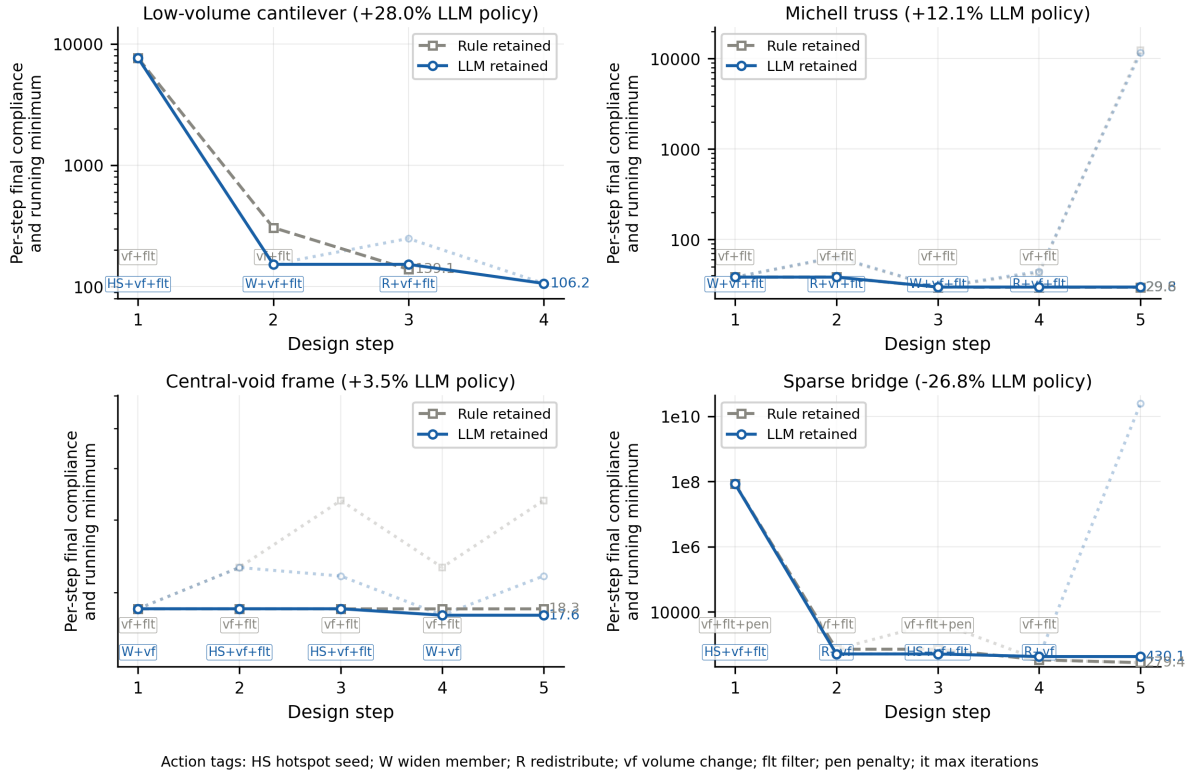
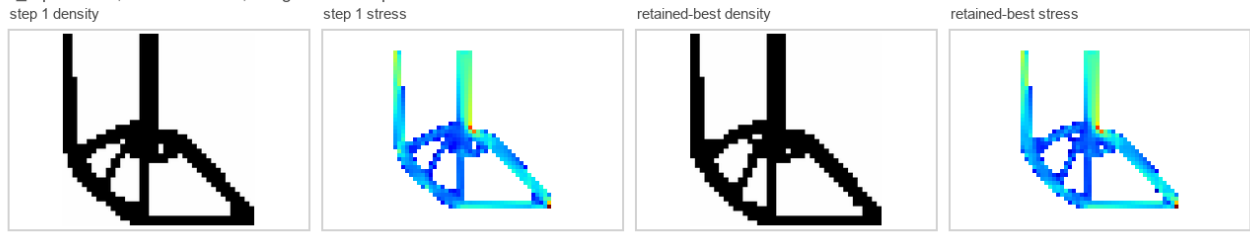


Figure 11: Step-by-step compliance convergence for seed-42 traces ($\sigma_{\text{yield}} = 120.3$). Faint lines show raw per-step final compliance; bold lines show the retained running minimum used by the trace-level selection rule. The small action tags identify applied controller actions (HS=hotspot seed, W=widen member, R=redistribute, vf=volume fraction, flt=filter radius, pen=penalization). The logarithmic y-axis keeps exploratory spikes visible. Scalar tables instead report retained-best compliance aggregated over three seeds.

Figure 12 shows the controller sequence for a representative L-bracket repeat with seed 42. Under this trace, both the soft-seed LLM condition and the rule-based condition pass all seven gate checks. The figure is therefore used as a controller-sequence illustration rather than as evidence of a practical retained-compliance advantage: the density and stress fields show that the LLM action only slightly changes the retained L-bracket topology relative to the rule-based condition.

L-bracket: soft-seed controller, seed 42

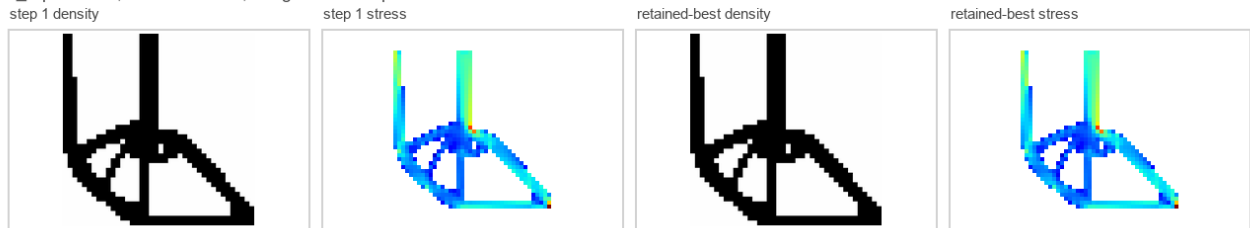
$C_{rep}=93.916$; final $C=93.916$; 7/7 gate checks passed



(a) Soft-seed LLM condition: step 1 and retained-best density/stress fields for the L-bracket controller sequence. The final state passes all seven gate checks, with $C_{rep} = 93.916$.

L-bracket: rule-based controller, seed 42

$C_{rep}=93.991$; final $C=93.991$; 7/7 gate checks passed



(b) Rule-based condition: step 1 and retained-best density/stress fields for the matched L-bracket run. The final state passes all seven gate checks, with $C_{rep} = 93.991$.

Figure 12: Controller sequence for the L-bracket in the primary seed-42 evaluation run ($\sigma_{yield} = 120.3$, seed 42). The panels show step 1 density, step 1 von Mises stress, retained-best density, and retained-best von Mises stress.

Figure 13 provides the analogous density-and-stress comparison for the Michell truss, the most geometrically nuanced problem in the suite. The three-seed soft-seed mean is lower than rule-based compliance (26.05 vs. 29.64), although seed-level behavior remains variable. The visual comparison shows the geometry and stress-field differences behind that aggregate result.

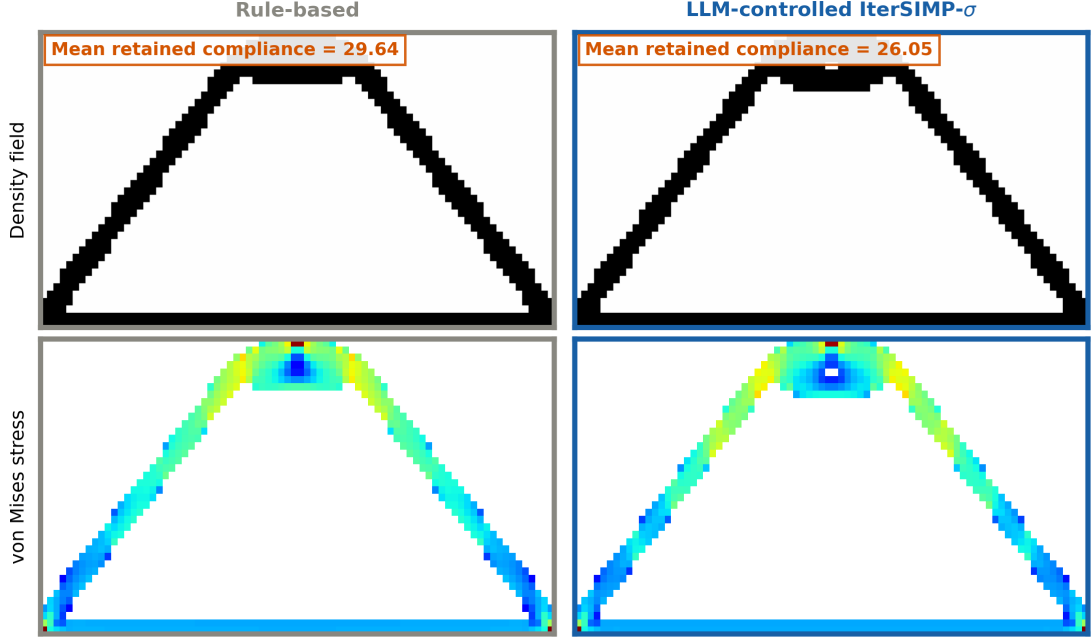


Figure 13: Representative seed-42 density and von Mises stress fields for the Michell truss ($\sigma_{\text{yield}} = 120.3$). Labels report three-seed mean retained-best compliance C_{rep} : rule-based (left, $C = 29.64$) vs. soft-seed LLM (right, $C = 26.05$, 12.1% lower retained compliance). Stress colors are normalized per panel.

5.5 Variance and high-CV problems

Rule-based compliance is nearly deterministic across seeds (median CV = 0.0%), reflecting the absence of stochastic elements in the rule-based action sequence once the SIMP solver follows a deterministic initialization and controller state. Soft-seed compliance is stable on 11 of 16 problems (CV < 5%). The largest observed variability occurs on the sparse bridge (CV = 23.9%), Michell truss (12.1%), portal frame (12.0%), asymmetric low-volume cantilever (6.4%), and bridge with circular void (5.3%). Figures 14–16 provide seed-level visual comparisons for representative cases in the figure set.

MBB beam (CV = 0.01%, Figure 14): all three soft-seed repeats converge to nearly identical compliance ($C = 154.48, 154.47, 154.52$). The soft-seed condition is therefore a small rule-based loss on this problem rather than a bimodal success case.

Low-volume cantilever (CV = 4.5%, Figure 15): all three repeats pass all seven gate checks, with compliance values $C = 105.83, 95.18, \text{ and } 98.02$. The spread reflects modest initialization sensitivity within the same broad X-truss basin.

Michell truss (CV = 12.1%, Figure 16): the three repeats give $C = 29.80, 26.25, \text{ and } 22.08$; the first final state fails gate checks and the latter two pass all seven gate checks. The mean is lower than rule-based compliance, but the seed-level feasibility and compliance variation should be treated as material uncertainty.

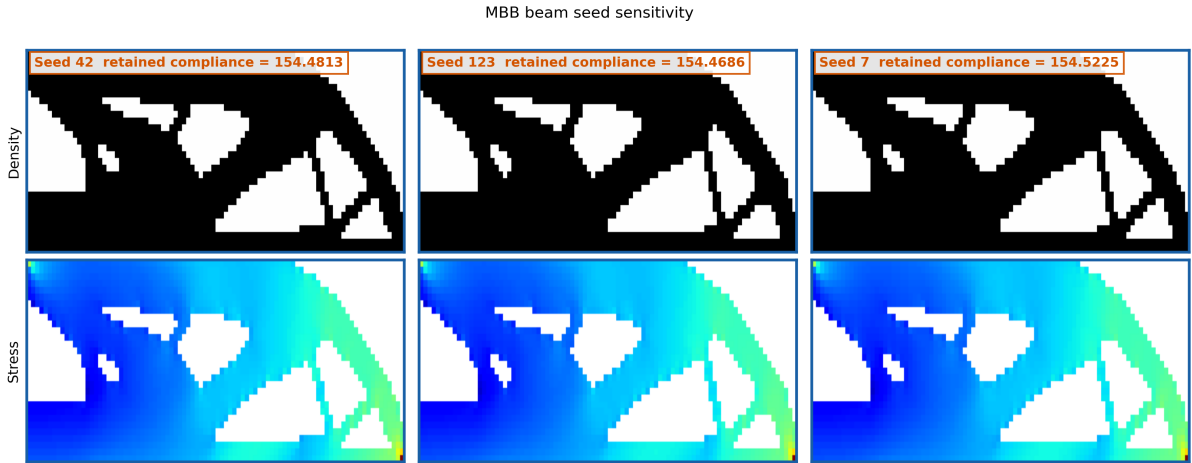


Figure 14: **MBB beam** seed sensitivity ($CV = 0.01\%$). All three soft-seed repeats are nearly identical ($C = 154.48, 154.47, 154.52$), producing slightly lower rule-based retained compliance rather than a soft-seed advantage.

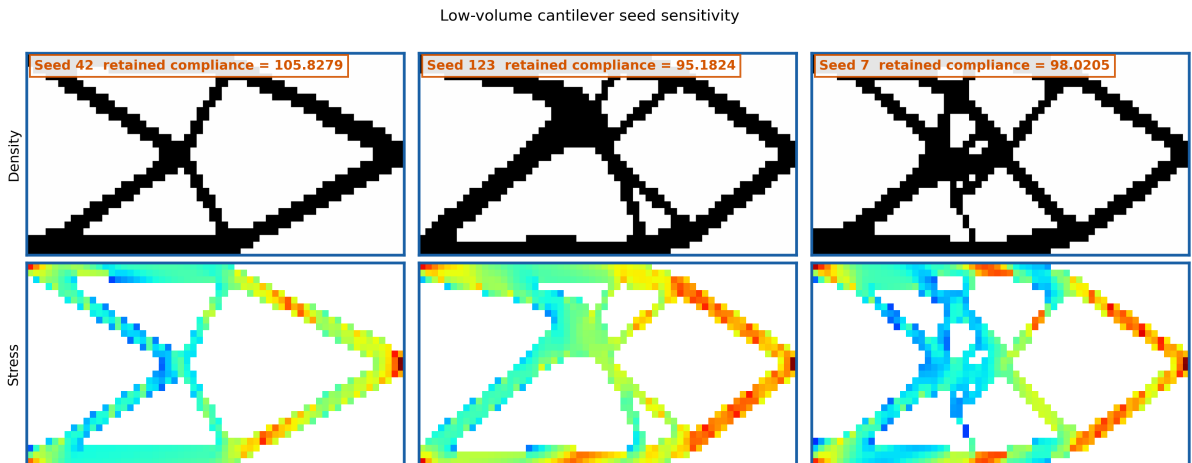


Figure 15: **Low-volume cantilever** seed sensitivity ($CV = 4.5\%$). The three soft-seed repeats pass all seven gate checks with $C = 105.83, 95.18, \text{ and } 98.02$.

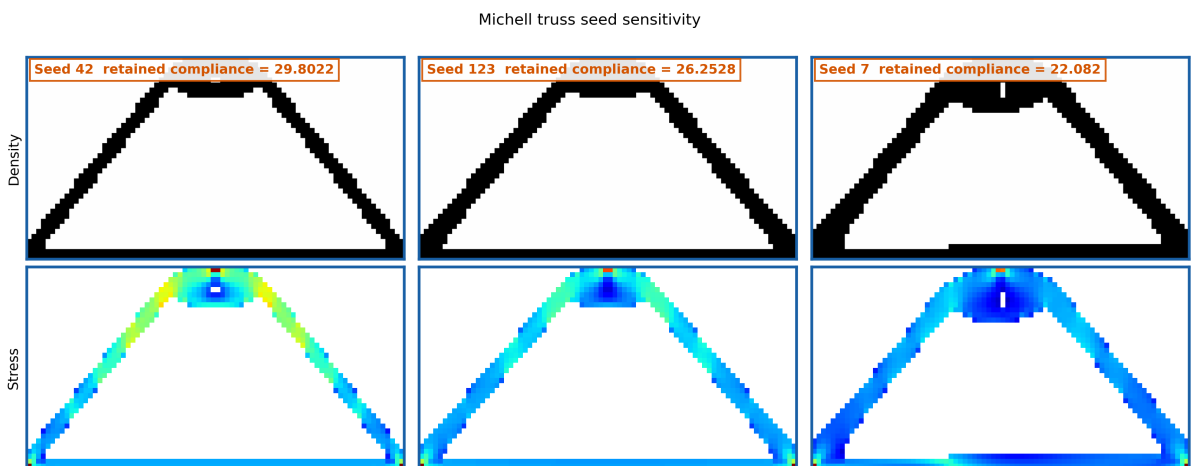


Figure 16: **Michell truss** seed sensitivity ($CV = 12.1\%$). The three soft-seed repeats give $C = 29.80, 26.25, \text{ and } 22.08$; the first final state fails gate checks and the latter two pass all seven gate checks. Figures 14–16 together constitute the seed sensitivity analysis (LLM condition; density top row, von Mises stress bottom row, seeds 42/123/7 left to right).

5.6 3D benchmark

Table 9 reports the exploratory controller-policy results for the six three-dimensional problems under the same paper-wide threshold $\sigma_{\text{yield}} = 120.3$. Both conditions pass all seven gate checks on all six reported summaries. In this exploratory subset, the LLM controller-policy condition has lower retained compliance on 4 of 6 problems and ties the remaining 2, but these differences should not be read as fixed-volume compliance reductions: the controller changes the volume-fraction target on several 3D traces. The bridge row uses a validity-filtered bridge evaluation for the same benchmark setting satisfying the predefined finite-positive-compliance and seven-gate validity criteria in Appendix A. Because this 3D subset does not include fixed-volume attribution studies or a no-seed 3D ablation, it is controller-level evidence rather than an isolated estimate of the seed materialization effect.

Table 9: 3D benchmark: LLM vs. rule-based, $\sigma_{\text{yield}} = 120.3$. Entries are three-seed means of retained-best compliance C_{rep} ; descriptive population standard deviations are zero for these 3D scalar summaries and are omitted. Final vf gives the final volume-fraction target for LLM/rule traces. The three 3D scalar repeats were identical under the recorded deterministic controller/solver paths, so these repeats should be read as trace reproducibility checks rather than independent stochastic samples. Both conditions pass all seven gate checks on all 6 reported summaries. Δ : relative retained-compliance difference = $(C_{\text{rule}} - C_{\text{LLM}})/C_{\text{rule}} \times 100\%$. The 3D bridge LLM value and visual panels use the validity-filtered bridge evaluation checked in Appendix A; the original run failed the predefined finite-positive-compliance validity criterion. The 3D bridge rule value uses the lower final state because that logged endpoint satisfies the same finite-positive, grayness, and seven-gate validity checks as the retained tracker. This is not a fixed-volume comparison and should not be interpreted as a validated 3D performance claim. Lower retained compliance under the LLM policy: 4/6; ties: 2/6.

Problem	Mesh	n_e	C_{rep}		Δ (%)	Steps		Final vf L/R	Class
			LLM	Rule		LLM	Rule		
3D cantilever	40×20×10	8000	4.884	5.916	+17.4	2	1	0.31/0.25	LLM
3D MBB beam	40×14×6	3360	30.431	38.349	+20.6	2	1	0.24/0.18	LLM
3D bridge	30×10×6	1800	3.058	3.201	+4.4	5	2	0.32/0.26	LLM
3D L-bracket	20×20×5	2000	11.859	11.859	0.0	1	1	0.25/0.25	Tie
3D Michell truss	24×12×6	1728	3.341	4.400	+24.1	2	1	0.18/0.12	LLM
3D torsion block	20×10×8	1600	4.887	4.887	0.0	1	1	0.18/0.18	Tie
Lower retained compliance under LLM policy: 4/6			Ties: 2/6						
Summed mean runtime over six problems (s):			6075 vs 2196		+177%				

Figure 17 shows isosurface renderings and von Mises stress fields for the four non-tie 3D problems; Figure 18 provides matching density and density-slice comparisons for the same four problems.

These 3D results should be interpreted with caution because the stress gate is not separately calibrated for 3D and the comparison is not fixed-volume. *Mechanistic limitation*: in the recorded 3D traces, 3D hotspot and member-widening actions add circular seed regions extruded through depth rather than spherical volumetric seeds. The LLM policy also changes global parameters, including volume fraction, filter radius, and penalization. The retained-compliance differences in Table 9 therefore cannot be attributed uniquely to seed materialization. The mean 3D runtime across the reported runs is 6075 s for the LLM controller and 2196 s for rule-based control, a +177% overhead.

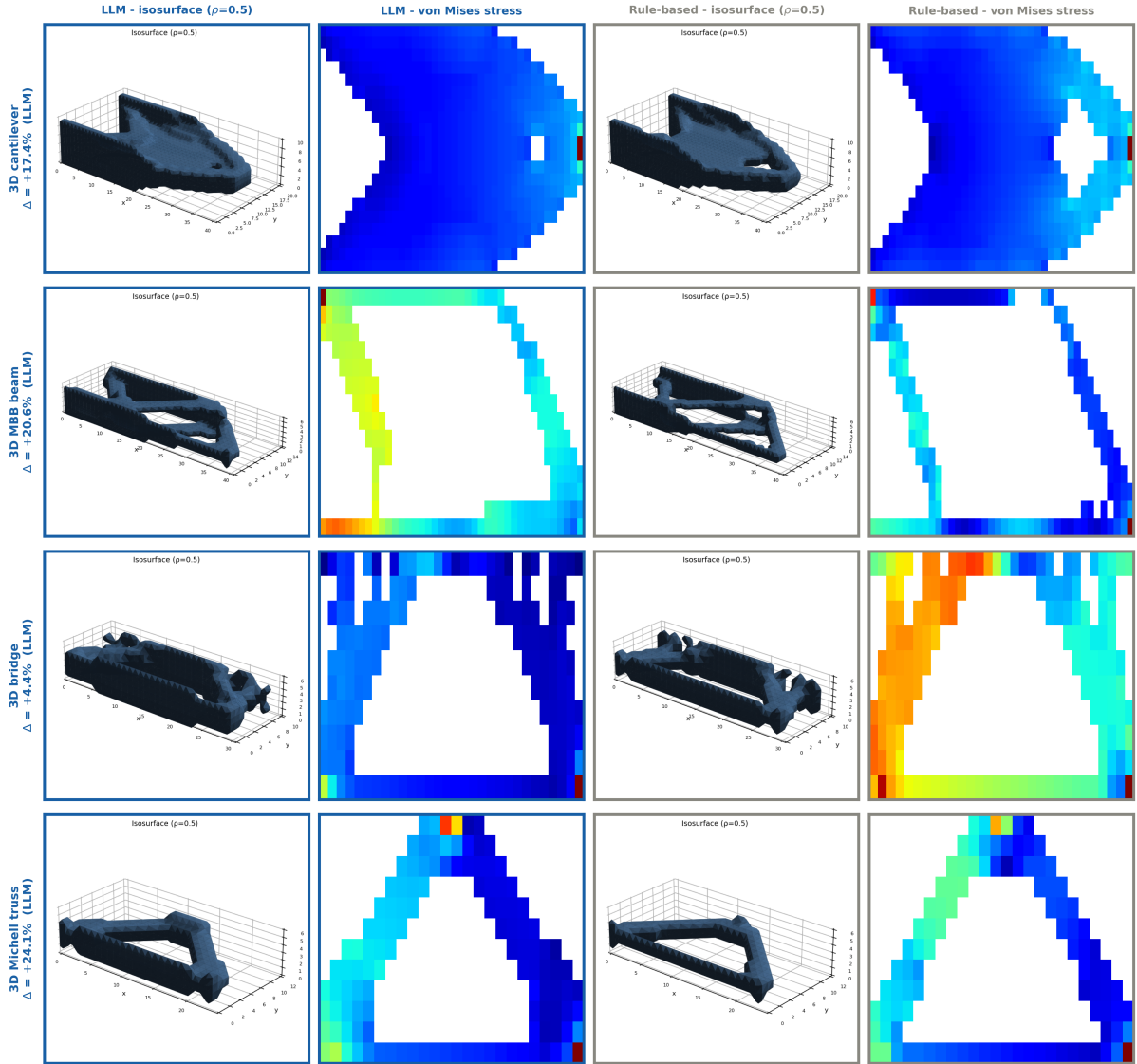


Figure 17: Isosurface renderings ($\rho_e = 0.5$ threshold) and von Mises stress fields for the four non-tie 3D benchmark problems. Images are seed-42 examples; compliance percentages use three-seed mean retained-best compliance C_{rep} . Left two columns: LLM (blue border); right two columns: rule-based (gray border). Stress colors are normalized per panel and are qualitative within-panel visualizations only; the 3D bridge LLM row uses the validity-filtered bridge evaluation checked in Appendix A.

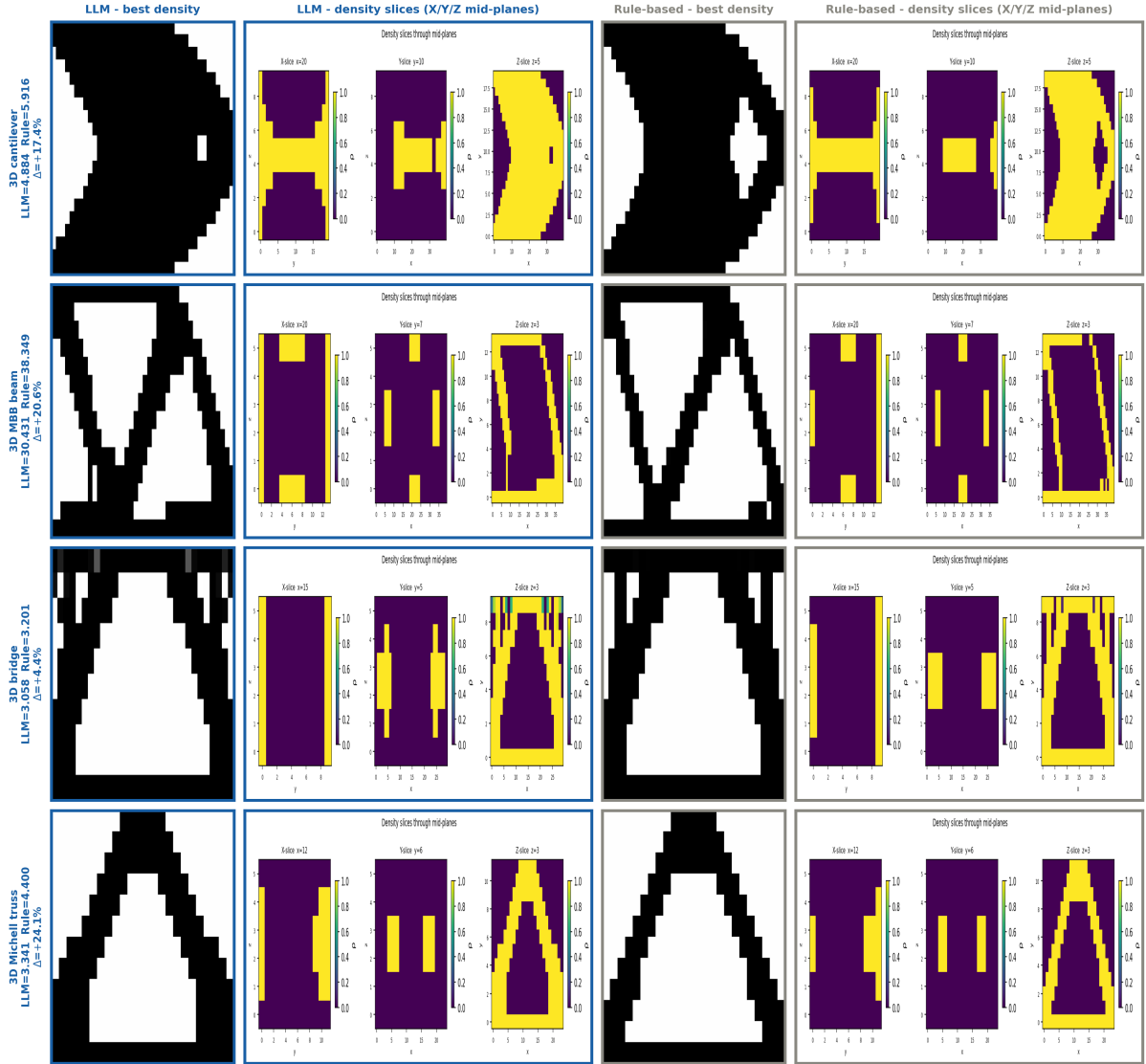


Figure 18: Representative seed-42 density fields and density slices through mid-planes (X, Y, Z) for the four non-tie 3D benchmark problems ($\sigma_{yield} = 120.3$). Scalar labels use three-seed mean retained-best compliance C_{rep} . LLM (blue border) vs. rule-based (gray border). The 3D bridge LLM panels use the validity-filtered bridge evaluation passing the predefined gate checks in Appendix A.

6 Ablation Study

6.1 Three-condition comparison

Figure 19 summarizes all 16 two-dimensional problems, while Table 10 reports representative cases where the three conditions produce meaningfully different outcomes. The values are three-seed means from the reported ablation summaries.

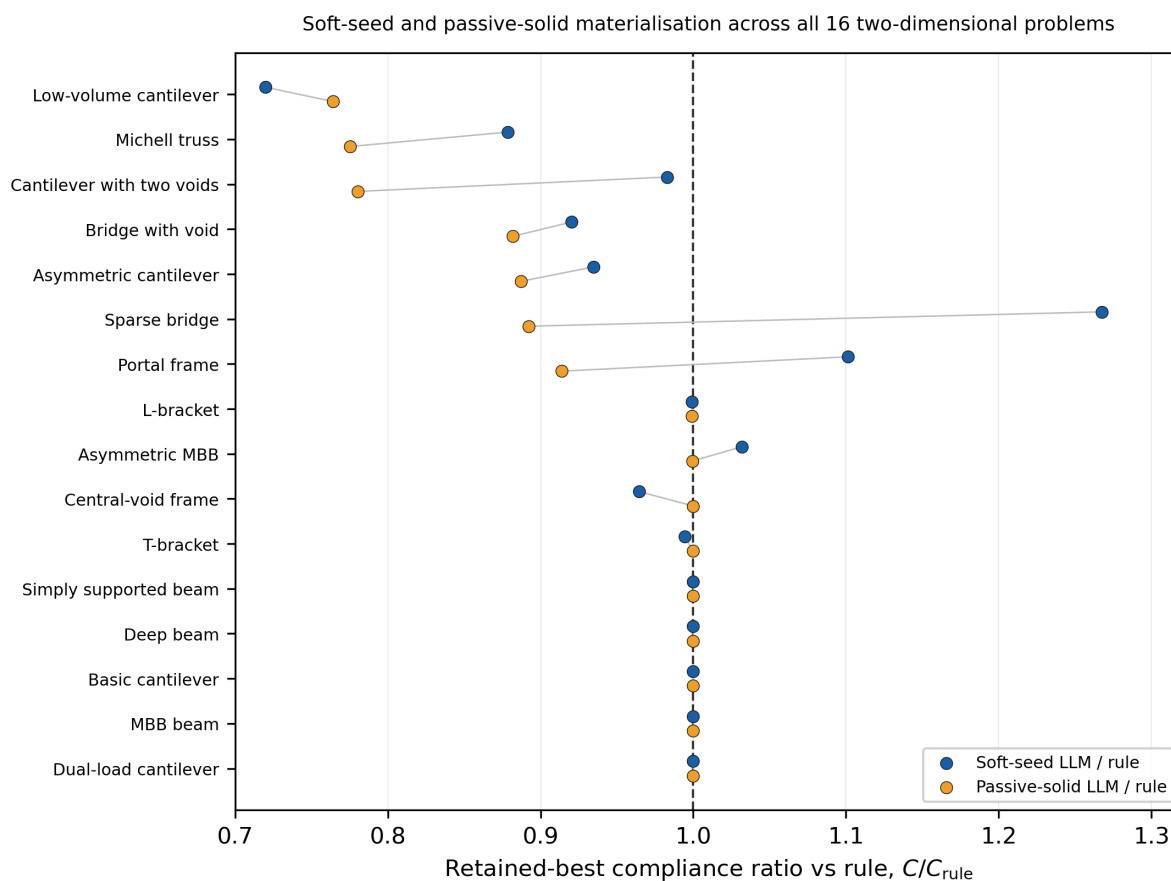


Figure 19: Three-way ablation summarized as retained-compliance ratios for all 16 two-dimensional problems. Blue points show soft-seed LLM divided by rule-based retained-best compliance; amber points show passive-solid LLM divided by rule-based retained-best compliance. Values below one are lower than the rule-based controller. The plot makes visible that passive-solid materialization is the stronger aggregate condition, while soft seeding is the less restrictive mechanism.

Table 10: Three-way ablation at $\sigma_{\text{yield}} = 120.3$. Soft-seed LLM: soft density seeding. Passive-solid LLM: passive-solid seeding. Rule: rule-based. Δ columns: relative retained-compliance differences; positive values denote lower retained compliance for the left named condition.

Problem	Soft LLM	Solid LLM	Rule	Δ soft vs rule	Δ soft vs solid
Low-volume cantilever	99.7	105.8	138.5	+28.0%	+5.8%
Michell truss	26.0	23.0	29.6	+12.1%	-13.3%*
Central-void frame	17.6	18.3	18.3	+3.5%	+3.5%
Cantilever with two voids	115.2	91.5	117.2	+1.7%	-25.9%*
Portal frame	89.8	74.5	81.5	-10.1%	-20.5%*
Sparse bridge	371.9	261.8	293.4	-26.8%	-42.1%*
Geo. mean, all 16 problems:					
$C_{\text{soft}}/C_{\text{rule}}$			= 0.981	(+1.9%)	
$C_{\text{solid}}/C_{\text{rule}}$			= 0.926	(+7.4%)	
$C_{\text{soft}}/C_{\text{solid}}$					= 1.059 (-5.9%)

* Passive-solid seeding outperforms soft seeding on these problems. This is the main reason passive-solid intervention is the stronger aggregate condition in the reported data.

6.2 Ablation interpretation

Across all 16 problems, the geometric mean compliance ratios are:

$$\begin{aligned}
 C_{\text{soft}}/C_{\text{rule}} &= 0.981, \\
 C_{\text{solid}}/C_{\text{rule}} &= 0.926, \\
 C_{\text{soft}}/C_{\text{solid}} &= 1.059.
 \end{aligned} \tag{8}$$

These ratios do not support a positive additive decomposition in which soft seeding improves on passive-solid materialization. Instead, passive-solid intervention is the stronger aggregate condition in the reported data, while soft seeding remains mechanistically attractive because it does not remove optimizer freedom. Thus, in this benchmark, soft seeding is the less restrictive but weaker materialization mechanism, not the strongest controller-policy variant.

Per-problem behavior is mixed. Soft seeding is better than passive-solid materialization on the low-volume cantilever and central-void frame, but passive-solid materialization is better on the Michell truss, cantilever with two voids, portal frame, and sparse bridge. These cases motivate future work on adaptive seed persistence rather than a fixed choice between soft and frozen materialization.

7 Discussion

7.1 Stress constraint handling: outer-loop gating vs. gradient-based formulations

A fundamental design choice in IterSIMP- σ is that stress constraints are handled via an *outer design loop* rather than within the SIMP solver’s gradient computation. At each design step, the inner solver minimizes compliance only; a separate forward FEA pass then evaluates the per-element von Mises stress field, and the evaluator checks whether $\max_{e; \rho_e > 0.5} \sigma_{\text{vm}}^{(e)} \leq \sigma_{\text{yield}}$. If this gate fails, the LLM proposes a spatially targeted geometry modification and the solver is re-invoked on the updated specification.

This is a deliberate architectural choice, not an equivalence claim, and it has concrete consequences. The SIMP density update receives no gradient information about the stress field:

sensitivities $\partial\sigma_{\text{vm}}/\partial\rho_e$ are never computed, and the optimality-criteria update (Equation (6)) drives densities toward compliance reduction without direct knowledge of where stress concentrations are forming. In classical stress-constrained formulations—P-norm penalty [10, 11], augmented Lagrangian [13], or ε -relaxation [9]—the stress constraint enters the Lagrangian directly, and adjoint analysis provides element-wise stress sensitivity to guide the density update. These methods can resolve stress-feasible topologies in a single solve without an outer loop.

The rationale for our outer-loop approach is threefold. First, it preserves the unmodified SIMP solver as a black box, enabling the framework to wrap any existing density-based solver without modification to its adjoint computation or sensitivity filtering. Second, the LLM’s contribution is a form of visual, geometric intervention that is complementary to adjoint stress sensitivities: it identifies *where* a stress concentration appears in a rendered field and proposes a geometric fix at that location. Adjoint stress sensitivities tell the solver *how much* each element contributes to an aggregate stress measure; the visual controller supplies an interpretable spatial action vocabulary. Third, the outer-loop formulation naturally accommodates the soft density seed mechanism: geometry modifications are applied to the problem specification between solver calls, and the seed initialization biases the next solve without constraining it.

The limitation is equally clear: when the stress constraint is tight (Section 7.2), the five-step outer loop may be insufficient to drive peak stress below σ_{yield} through geometry modifications alone, whereas a gradient-based formulation would continuously adjust densities toward stress feasibility. The deterministic calibration study (Table 8) is consistent with this limitation: at $q = 40$ ($\sigma_{\text{yield}} = 110.4$), both conditions fail on 6 of 16 problems because the compliance-only topology violates the stress gate by too wide a margin for spatial seeding to resolve within the step budget.

A natural extension—combining the LLM’s spatial targeting with a gradient-based stress-constrained inner solver—would address this limitation by providing adjoint stress sensitivity within each solve while using the LLM to propose inter-solve geometry modifications for concentrations that persist across continuation steps. We leave this integration to future work.

7.2 Operating window

The deterministic calibration study identifies a moderate stress-gate range ($\sigma_{\text{yield}} \in [120, 149]$, calibration percentile $q \in [50, 55]$) in which roughly half the 2D problems fail the compliance-only stress gate. Below this range, constraints are tight enough that neither spatial seeding nor volume-fraction adjustments can satisfy the hardest cases within five design steps. Above it, the gate becomes loose and additional spatial reasoning is less likely to be repaid.

This operating window is consistent with the architectural role of an outer-loop spatial meta-heuristic: it is most relevant when the compliance-only topology is close to stress-feasible but requires localized geometric corrections.

7.3 Mesh resolution and scalability

The benchmark problems in this study use relatively coarse meshes (1,600–8,000 elements), which are sufficient for an exploratory evaluation of the LLM spatial targeting mechanism but below the resolution of production-scale stress-constrained topology optimization studies that routinely employ 10,000–100,000 elements [12–14]. At coarse resolution, stress concentrations are partially smoothed by the mesh itself, potentially understating the difficulty of the stress constraint. The current 3D cases are therefore exploratory small-mesh tests and do not establish scalability.

The scalability of IterSIMP- σ is governed by two factors: the SIMP solver’s FEA cost, which grows with the number of elements n_e , and the LLM call cost. The interpreter receives fixed-resolution 300×300 images regardless of the underlying mesh, so API latency is less directly tied to mesh size than the FEA cost. The LLM overhead would therefore be expected to

become a smaller fraction of total wall time if FEA cost dominates at higher mesh resolution. Empirically, the 3D benchmark (up to 8,000 elements) shows lower retained compliance for the LLM controller-policy condition on 4 of 6 problems and ties on 2, but this should not be read as an isolated validation of 3D seed materialization because no matched no-seed 3D ablation is included. Validation at higher resolutions and with a separately calibrated 3D stress gate remains an important direction for future work.

7.4 Computational overhead

The soft-seed LLM condition incurs an +88% wall-time overhead over rule-based control on the 16 two-dimensional problems (about 11.4 min vs 6.0 min in summed mean runtime on CPU). The additional wall time is consistent with one hosted-model call per design step ($\approx 5\text{--}10$ s in observed interactive use), but per-call provider latency was not persisted in the traces. The additional FEA pass for stress computation adds approximately one solver iteration equivalent. The reported primary comparison comprises 66 LLM-controller runs and 66 matched rule-based runs (48 2D and 18 3D runs per condition); the 3D bridge LLM value uses the validity-filtered bridge evaluation checked in Appendix A. Trace and action counts are reported in Appendix A. The summed recorded wall time is 20,272 s (5.63 h) for the LLM traces and 7,676 s (2.13 h) for the rule-based traces on the CPU-only Windows workstation documented in the computational-environment notes and summarized in Appendix A. Exact model-service token counts, per-call latency distribution, energy use, retention settings, and served model revision are not available from the archived records, so exact hosted-model replay is not possible. This overhead is material and should be reduced by batching API calls, skipping interpreter calls once gates pass, or using locally hosted models.

7.5 Failure modes and future directions

Four failure patterns were identified: high seed sensitivity on some 2D problems, geometric imprecision in seed placement, soft-seed erosion when a persistent reinforcement would be beneficial, and stress saturation under very tight constraints ($q \leq 45$), where the compliance-only topology violates the stress gate by too wide a margin for five design steps to resolve.

The fixed-volume 2D study controls the largest material-budget confound and adds direct localization measurements, but it does not close the causal question. Feasible-final scoring is mixed, deterministic hotspot seeding is competitive, several policies improve retained-any compliance without a matching feasible-primary advantage, and the LLM condition has incomplete execution/trace coverage. The next evidence tier is therefore not additional prompt tuning; it is comparison against a stress-aware inner solver such as P-norm, K-S, or augmented Lagrangian stress optimization, followed by separately calibrated fixed-volume 3D reruns and mesh-refinement checks.

7.6 Relationship to prior work

Compared to the compliance-only predecessors [36, 37], which operated on a single density image and used only passive void/solid regions, the stress-gated extension introduces two key advances: the dual-image interpreter that conditions on both density and stress fields simultaneously, and the soft density seed mechanism that preserves optimizer freedom (Section 5.6 discusses the 3D attribution limits). More specifically, the earlier adaptive-continuation work studied compliance-only schedule control, while AutoSiMP studied natural-language problem configuration and end-to-end setup; neither evaluates dual density–stress visual inputs, local stress-violation localization, stress-gated spatial actions, or the fixed-volume attribution tests reported here. The ablation in Section 6 shows that the materialization choice is unresolved:

passive-solid intervention is stronger in aggregate, while soft seeding preserves optimizer freedom and remains the less restrictive mechanism for future stress-aware inner solvers.

8 Conclusion

We have presented IterSIMP- σ , an exploratory framework for stress-gated topology optimization in which an LLM agent interprets dual density-and-stress field images and proposes spatially targeted geometry modifications via an outer design loop that wraps an unmodified compliance-only SIMP solver. The current evidence supports a narrower claim than a general performance-method claim: LLM spatial proposals are technically implementable and inspectable, with selected cases showing benefit, but the fixed-volume study does not establish visual reasoning as the causal source of performance improvement.

The key results are: (i) the soft-seed LLM condition gives a modest 1.9% lower geometric-mean retained compliance than rule-based control on the 16 2D problems, under controller policies that can change final volume fraction, but the two-sided Wilcoxon test is not significant ($W = 33$, $p = 0.382$; one-sided $p = 0.191$); when the recorded traces are re-scored under feasible-retained and feasible-final metrics, infeasible runs are excluded rather than counted as wins, leaving five and six incomplete 2D pairs respectively; (ii) the passive-solid LLM condition gives a larger 7.4% lower geometric-mean retained compliance than rule-based control, but it achieves this by freezing LLM-placed material and is therefore a more restrictive mechanism than soft seeding; (iii) the fixed-volume 2D study gives lower LLM feasible-retained compliance than rule-based control in 5 of 9 complete paired problems; 44 of 48 LLM attempted slots completed a design evaluation, 25 of those 44 completed evaluations have an all-gate-passing retained state, and 27 of 48 rule-based evaluations have an all-gate-passing retained state, feasible-final scoring is split 4/4/1, and deterministic max-stress hotspot seeding remains competitive; (iv) direct localization over 76 accepted LLM spatial actions with per-step records gives mean normalized seed-to-hotspot distance 0.221 and mean overlap with the top 1%, 5%, and 10% stress regions of 0.041, 0.118, and 0.196, so the current evidence does not prove precise visual hotspot localization; (v) several soft-seed cases have lower retained compliance, most notably the low-volume cantilever (+28.0%), Michell truss (+12.1%), bridge with circular void (+8.0%), and asymmetric low-volume cantilever (+6.5%), but these are retained-best controller-policy differences rather than feasible-final fixed-volume wins; (vi) the six-problem 3D study remains exploratory controller-level evidence, not a fixed-volume or separately calibrated 3D validation; and (vii) the 2D computational overhead is +88% in wall time and the 3D subset has about +177% summed runtime overhead, so the current system should be read as an inspectable design-assist and spatial-proposal framework rather than an efficient optimizer, although per-call provider latency was not persisted.

The stress constraint in IterSIMP- σ is handled as an outer-loop gate check rather than through gradient-based constraint handling within the solver. This preserves solver modularity and motivates further study of whether LLM-guided spatial interventions can complement established adjoint-based methods. Integrating LLM spatial targeting with gradient-based stress-constrained formulations is a natural next step that could combine the spatial-action traces studied here with the continuous sensitivity guidance that adjoint methods provide.

Code availability

The full code release will be made available after the arXiv preprint is online at the [project GitHub repository](#). It will include runnable code, environment files, experiment drivers, figure-generation scripts, smoke tests, compact result summaries, and a comprehensive README for reproducing the reported and extended experiments. No external dataset is used. The release

is intended for code-level reproduction and new reruns; it will include the scripts and compact result summaries needed to reproduce the reported figures and tables. It will also include prompt templates, action-validation logic, and the redacted audit-record schema used by new API-backed reruns to retain rendered inputs, provider outputs, parsed actions, and solver-state summaries. Exact replay of the original hosted-model calls is not available because complete provider I/O records, response identifiers, served-model revision metadata, and retention settings were not archived.

Ethics and data-transfer note

The experiments use synthetic structural benchmark fields and no human-subject or personal data. LLM-controlled runs send rendered density and stress images plus accompanying text and numerical prompts to a hosted model; proprietary applications should use available data-retention controls or a local/on-premise vision model. Provider energy use was not observable, so the paper reports local wall-clock timing only. Controller outputs are research evaluations and require conventional engineering verification before safety-critical design use.

Funding

This research was supported by startup funding from Santa Clara University.

Declaration of competing interest

The authors declare that they have no known competing financial interests or personal relationships that could have appeared to influence the work reported in this paper.

A Reproducibility Map and Metric Definitions

Table 11 maps the manuscript-level claims to the evidence used to generate them. The scalar tables use C_{rep} as defined in Section 4; this is a retained-best diagnostic metric, not a feasibility-conditioned primary performance metric. C_{final} is retained in the per-step records and is reported only in explicitly labeled feasible-final re-scores and fixed-volume endpoints.

The reported 3D bridge LLM row uses a validity-filtered bridge evaluation for the same benchmark setting that passes the predefined finite-positive-compliance validity criterion. An earlier 3D bridge run had a nonphysical retained-compliance value and is excluded from the scalar table and visual panels.

Regeneration commands and checksums are provided with the released code rather than duplicated in the article body.

Table 11: Compact reproducibility map for the reported claims.

Paper element	Evidence used for reporting
Main 2D and exploratory 3D scalar tables	Retained-best compliance summary with final gate-pass counts reported separately. The 3D bridge row uses a validity-filtered bridge evaluation.
Feasibility-conditioned re-score	Existing-trace feasibility table; infeasible traces are excluded from feasible-retained and feasible-final means.
Fixed-volume 2D attribution study	Fixed-volume summary and tables; endpoint tables separate attempted slots, completed evaluations, missing executions, and feasible completed evaluations. Recovered scalar records without per-step traces are excluded from localization diagnostics.
Sensitivity and ablation analyses	Sensitivity, Wilcoxon, and mechanism-ablation summaries.
Figure panels	Figure assets generated from the reported summaries and retained trace images; representative galleries use seed-42 examples unless stated otherwise.
Model/runtime configuration	Gemini 3.1 Flash-Lite Preview at temperature 0, seeds 42/123/7, Python 3.11.5, NumPy 1.24.3, SciPy 1.11.1, Matplotlib 3.7.2, Pillow 9.4.0, Windows 10.0.26200, Intel Core i9-13900KF, 32 logical processors, and 95.85 GiB visible memory.
Hosted-model replay scope	The archived records retain parsed prompts/action summaries and solver state, but not complete provider input/output records, provider response identifiers, served-model revision metadata, or retention settings.

Table 12: Reader-facing metric definitions used in the paper.

Metric	Meaning
Retained-best compliance, C_{rep}	Retained-best compliance across design steps; this is the scalar used in the compliance tables and geometric means and is not necessarily an all-check-passing state.
Final-state compliance, C_{final}	Compliance of the last solver state in a trace; available for inspection but not used in the scalar tables unless explicitly stated.
Gate-pass status	The final state passes all seven gate checks. Four informational diagnostics are recorded separately and do not gate validity.
Population standard deviation	Descriptive standard deviation over the three repeats; it is not an inferential uncertainty estimate.

Table 13: Evaluation availability and controller-action counts for fixed-volume localization diagnostics.

Condition	Evaluations with records	Accepted controller actions	Rejected or inadmissible actions
Soft-seed LLM	28	84	0
Exact hotspot	47	148	0
Rule-based controller	48	78	0
Random stress region	48	155	0
Density-only LLM	48	141	0
Stress-only LLM	48	150	0
Numeric-only LLM	48	144	0
Global-only LLM	48	81	0

Accepted controller actions include all accepted actions recorded in per-step records. Localization statistics in the main text and figures use the accepted spatial-action subset; for the soft-seed LLM condition this subset contains 76 spatial actions over 28 completed evaluations with per-step records.

Table 14: Initial and final volume-fraction targets for the 2D primary controller-policy comparison. Values are means over three traces; parentheses list distinct final targets when repeats differ.

Problem	Initial v_f	Soft-seed LLM final v_f	Rule-based final v_f
Asymmetric low-volume cantilever	0.18	0.56	0.50
Sparse bridge	0.18	0.56	0.50
Bridge with circular void	0.25	0.61 (0.57/0.63)	0.57
Low-volume cantilever	0.12	0.33 (0.29/0.35)	0.28
Basic cantilever	0.35	0.35	0.35
Cantilever with two voids	0.25	0.28	0.28
Deep beam	0.35	0.35	0.35
Dual-load cantilever	0.30	0.46	0.46
Central-void frame	0.22	0.18	0.12
L-bracket	0.30	0.30	0.30
Asymmetric MBB beam	0.30	0.59 (0.54/0.62)	0.62
MBB beam	0.35	0.67	0.67
Michell truss	0.15	0.16 (0.08/0.20)	0.08
Portal frame	0.22	0.25 (0.18/0.22/0.36)	0.30
Simply supported beam	0.30	0.30	0.30
T-bracket	0.25	0.17 (0.15/0.21)	0.15

References

- [1] Martin P. Bendsøe and Ole Sigmund. *Topology Optimization*. Springer, Berlin, 2004. doi: 10.1007/978-3-662-05086-6.
- [2] Ole Sigmund and Kurt Maute. Topology optimization approaches. *Structural and Multidisciplinary Optimization*, 48(6):1031–1055, 2013. doi: 10.1007/s00158-013-0978-6.
- [3] Martin P. Bendsøe and Noboru Kikuchi. Generating optimal topologies in structural design using a homogenization method. *Computer Methods in Applied Mechanics and Engineering*, 71(2):197–224, 1988. doi: 10.1016/0045-7825(88)90086-2.
- [4] Ole Sigmund. A 99 line topology optimization code written in Matlab. *Structural and Multidisciplinary Optimization*, 21(2):120–127, 2001. doi: 10.1007/s001580050176.
- [5] Erik Andreassen, Anders Clausen, Mattias Schevenels, Boyan S. Lazarov, and Ole Sigmund. Efficient topology optimization in MATLAB using 88 lines of code. *Structural and Multidisciplinary Optimization*, 43(1):1–16, 2011. doi: 10.1007/s00158-010-0594-7.
- [6] Fengwen Wang, Boyan S. Lazarov, and Ole Sigmund. On projection methods, convergence and robust formulations in topology optimization. *Structural and Multidisciplinary Optimization*, 43(6):767–784, 2011. doi: 10.1007/s00158-010-0602-y.
- [7] Boyan S. Lazarov and Ole Sigmund. Filters in topology optimization based on Helmholtz-type differential equations. *International Journal for Numerical Methods in Engineering*, 86(6):765–781, 2011. doi: 10.1002/nme.3072.
- [8] Ole Sigmund and Joakim Petersson. Numerical instabilities in topology optimization: a survey on procedures dealing with checkerboards, mesh-dependencies and local minima. *Structural Optimization*, 16(1):68–75, 1998. doi: 10.1007/BF01214002.
- [9] Pierre Duysinx and Martin P. Bendsøe. Topology optimization of continuum structures with local stress constraints. *International Journal for Numerical Methods in Engineering*, 43(8):1453–1478, 1998. doi: 10.1002/(SICI)1097-0207(19981230)43:8<1453::AID-NME480>3.0.CO;2-2.
- [10] Chau Le, Julian Norato, Tyler Bruns, Christopher Ha, and Daniel Tortorelli. Stress-based topology optimization for continua. *Structural and Multidisciplinary Optimization*, 41(4): 605–620, 2010. doi: 10.1007/s00158-009-0440-y.

- [11] R. J. Yang and C. J. Chen. Stress-based topology optimization. *Structural Optimization*, 12(2–3):98–105, 1996. doi: 10.1007/BF01196941.
- [12] Erik Holmberg, Börje Torstenfelt, and Anders Klarbring. Stress constrained topology optimization. *Structural and Multidisciplinary Optimization*, 48(1):33–47, 2013. doi: 10.1007/s00158-012-0880-7.
- [13] Fernando V. Senhora, Oliver Giraldo-Londoño, Ivan F. M. Menezes, and Glaucio H. Paulino. Topology optimization with local stress constraints: a stress aggregation-free approach. *Structural and Multidisciplinary Optimization*, 62(4):1639–1668, 2020. doi: 10.1007/s00158-020-02573-9.
- [14] Gustavo Assis da Silva, Niels Aage, André T. Beck, and Ole Sigmund. Three-dimensional manufacturing tolerant topology optimization with hundreds of millions of local stress constraints. *International Journal for Numerical Methods in Engineering*, 122(2):548–578, 2021. doi: 10.1002/nme.6548.
- [15] Fernando V. Senhora, Ivan F. M. Menezes, and Glaucio H. Paulino. Topology optimization with local stress constraints and continuously varying load direction and magnitude: towards practical applications. *Proceedings of the Royal Society A: Mathematical, Physical and Engineering Sciences*, 479(2271):20220436, 2023. doi: 10.1098/rspa.2022.0436.
- [16] Gustavo Assis Da Silva and Hélio Emmendoerfer Jr. Stress-constrained topology optimization with the augmented lagrangian method: A comparative study of subproblem solvers. *International Journal for Numerical Methods in Engineering*, 126(12):e70066, 2025. doi: 10.1002/nme.70066.
- [17] Tianshu Tang, Leijia Wang, Mingqiao Zhu, Huzhi Zhang, Jiarui Dong, Wenhui Yue, and Hui Xia. Topology optimization: a review for structural designs under statics problems. *Materials*, 17(23):5970, 2024. doi: 10.3390/ma17235970.
- [18] Matteo Bruggi and Pierre Duysinx. Topology optimization for minimum weight with compliance and stress constraints. *Structural and Multidisciplinary Optimization*, 46(3):369–384, 2012. doi: 10.1007/s00158-012-0759-7.
- [19] Oliver Giraldo-Londoño and Glaucio H. Paulino. A unified approach for topology optimization with local stress constraints considering various failure criteria: von Mises, Drucker–Prager, Tresca, Mohr–Coulomb, Bresler–Pister and Willam–Warnke. *Proceedings of the Royal Society A: Mathematical, Physical and Engineering Sciences*, 476(2238):20190861, 2020. doi: 10.1098/rspa.2019.0861.
- [20] Yonggyun Yu, Taeil Hur, Jaeho Jung, and In Gwun Jang. Deep learning for determining a near-optimal topological design without any iteration. *Structural and Multidisciplinary Optimization*, 59(3):787–799, 2019. doi: 10.1007/s00158-018-2101-5.
- [21] Ivan Sosnovik and Ivan Oseledets. Neural networks for topology optimization. *Russian Journal of Numerical Analysis and Mathematical Modelling*, 34(4):215–223, 2019. doi: 10.1515/rnam-2019-0018.
- [22] Zhenguo Nie, Tong Lin, Haoliang Jiang, and Levent Burak Kara. TopologyGAN: Topology optimization using generative adversarial networks based on physical fields over the initial domain. *Journal of Mechanical Design*, 143(3):031715, 2021. doi: 10.1115/1.4049533.
- [23] Changyu Deng, Yizhou Wang, Can Qin, Yun Fu, and Wei Lu. Self-directed online machine learning for topology optimization. *Nature Communications*, 13(1):388, 2022. doi: 10.1038/s41467-021-27713-7.

- [24] Jaydeep Rade, Aditya Balu, Ethan Herron, Jay Pathak, Rishikesh Ranade, Soumik Sarkar, and Adarsh Krishnamurthy. Algorithmically-consistent deep learning frameworks for structural topology optimization. *Engineering Applications of Artificial Intelligence*, 106:104483, 2021. doi: 10.1016/j.engappai.2021.104483.
- [25] Seungyeon Shin, Dongju Shin, and Namwoo Kang. Topology optimization via machine learning and deep learning: a review. *Journal of Computational Design and Engineering*, 10(4):1736–1766, 2023. doi: 10.1093/jcde/qwad072.
- [26] Yiming Zhang, Chen Jia, Hongyi Zhang, Naiyu Fang, Shuyou Zhang, and Nam H. Kim. Improving data-efficiency of deep generative model for fast design synthesis. *Journal of Mechanical Science and Technology*, 38(4):1957–1970, 2024. doi: 10.1007/s12206-024-0328-1.
- [27] Hongrui Chen, Aditya Joglekar, and Levent Burak Kara. Topology optimization using neural networks with conditioning field initialization for improved efficiency. *Journal of Mechanical Design*, 146(6):061702, 2024. doi: 10.1115/1.4064131.
- [28] Nikos A. Kallioras, Georgios Kazakis, and Nikos D. Lagaros. Accelerated topology optimization by means of deep learning. *Structural and Multidisciplinary Optimization*, 62(3): 1185–1212, 2020. doi: 10.1007/s00158-020-02545-z.
- [29] OpenAI. GPT-4 technical report, 2023. arXiv preprint arXiv:2303.08774.
- [30] Gemini Team, Rohan Anil, Sebastian Borgeaud, et al. Gemini: A family of highly capable multimodal models, 2023. arXiv preprint arXiv:2312.11805.
- [31] Liane Makatura, Michael Foshey, Bohan Wang, Felix Hähnlein, Pingchuan Ma, Bolei Deng, Megan Tjandrasuwita, Andrew Spielberg, Crystal Owens, Peter Yichen Chen, Allan Zhao, Amy Zhu, Wil Norton, Edward Gu, Joshua Jacob, Yifei Li, Adriana Schulz, and Wojciech Matusik. How can large language models help humans in design and manufacturing? Part 1: Elements of the LLM-enabled computational design and manufacturing pipeline. Harvard Data Science Review, Special Issue 5, 2024. URL <https://hdsr.mitpress.mit.edu/pub/15nqmdz1>.
- [32] Sizhong Qin, Hong Guan, Wenjie Liao, Yi Gu, Zhe Zheng, Hongjing Xue, and Xinzheng Lu. Intelligent design and optimization system for shear wall structures based on large language models and generative artificial intelligence. *Journal of Building Engineering*, 95: 109996, 2024. doi: 10.1016/j.jobee.2024.109996.
- [33] Haoran Liang, Mohammad Talebi Kalaleh, and Qipei Mei. Integrating large language models for automated structural analysis, 2025. arXiv preprint arXiv:2504.09754.
- [34] Bowen Zhang, Pengcheng Luo, Genke Yang, Boon-Hee Soong, and Chau Yuen. OR-LLM-Agent: Automating modeling and solving of operations research optimization problems with reasoning LLM, 2025. arXiv preprint arXiv:2503.10009.
- [35] Yan Zheng, Lida Zhang, Kaiwen Li, Rui Wang, Wenhua Li, Tao Zhang, Qingfu Zhang, and Yaochu Jin. A survey on large language models driven meta-optimizers for automated intelligent optimization. *Artificial Intelligence Review*, 59(2):72, 2026. doi: 10.1007/s10462-025-11470-w.
- [36] Shaoliang Yang, Jun Wang, and Yunsheng Wang. Large language models as optimization controllers: Adaptive continuation for SIMP topology optimization. arXiv preprint, 2026. arXiv:2603.25099.

- [37] Shaoliang Yang, Jun Wang, and Yunsheng Wang. AutoSiMP: Autonomous topology optimization from natural language via LLM-driven problem configuration and adaptive solver control. arXiv preprint, 2026. arXiv:2603.27000.
- [38] The Gemini Team. Gemini 3.1 flash-lite: Built for intelligence at scale. <https://blog.google/innovation-and-ai/models-and-research/gemini-models/gemini-3-1-flash-lite>, March 2026. Official Google model announcement; accessed 2026-04-28.
- [39] Shuzhi Xu, Jikai Liu, Bin Zou, Quhao Li, and Yongsheng Ma. Stress constrained multi-material topology optimization with the ordered SIMP method. *Computer Methods in Applied Mechanics and Engineering*, 373:113453, 2021. doi: 10.1016/j.cma.2020.113453.
- [40] Gustav Granlund, Mathias Wallin, Daniel Tortorelli, and Seth Watts. Stress-constrained topology optimization of structures subjected to nonproportional loading. *International Journal for Numerical Methods in Engineering*, 124(12):2818–2836, 2023. doi: 10.1002/nme.7230.
- [41] Gustavo Assis da Silva and Hélio Emmendoerfer. Fail-safe stress-constrained manufacturing error tolerant topology optimization. *Computer Methods in Applied Mechanics and Engineering*, 421:116817, 2024. doi: 10.1016/j.cma.2024.116817.
- [42] Grégoire Allaire and François Jouve. Minimum stress optimal design with the level set method. *Engineering Analysis with Boundary Elements*, 32(11):909–918, 2008. doi: 10.1016/j.enganabound.2007.05.007.
- [43] Xu Guo, Wei Sheng Zhang, Michael Yu Wang, and Peng Wei. Stress-related topology optimization via level set approach. *Computer Methods in Applied Mechanics and Engineering*, 200(47–48):3439–3452, 2011. doi: 10.1016/j.cma.2011.08.016.
- [44] Renato Picelli, Scott Townsend, Christopher Brampton, Julian Norato, and H. Alicia Kim. Stress-based shape and topology optimization with the level set method. *Computer Methods in Applied Mechanics and Engineering*, 329:1–23, 2018. doi: 10.1016/j.cma.2017.09.001.
- [45] Hélio Emmendoerfer and Eduardo A. Fancello. Topology optimization with local stress constraint based on level set evolution via reaction–diffusion. *Computer Methods in Applied Mechanics and Engineering*, 305:62–88, 2016. doi: 10.1016/j.cma.2016.02.024.
- [46] Liang Xia, Lin Zhang, Qi Xia, and Tielin Shi. Stress-based topology optimization using bi-directional evolutionary structural optimization method. *Computer Methods in Applied Mechanics and Engineering*, 333:356–370, 2018. doi: 10.1016/j.cma.2018.01.035.